JOURNAL OF PETROLOGY | VOLUME 53 | NUMBER 1 | PAGES 67–98 | 2012 | doi:10.1093/petrology/egr056

Evidence in Archaean Alkali Feldspar Megacrysts for High-Temperature Interaction with Mantle Fluids

EWA SŁABY[1]*, HERVÉ MARTIN[2,3,4], MORIHISA HAMADA[5], MICHAŁ ŚMIGIELSKI[6], ANDRZEJ DOMONIK[7], JENS GÖTZE[8], JOCHEN HOEFS[9], STANISŁAW HAŁAS[10], KLAUS SIMON[9], JEAN-LUC DEVIDAL[2], JEAN-FRANÇOIS MOYEN[11] AND MUDLAPPA JAYANANDA[12]

[1]INSTITUTE OF GEOLOGICAL SCIENCES, POLISH ACADEMY OF SCIENCES, RESEARCH CENTRE IN WARSAW, PL00-818 WARSAW, TWARDA 51/55, POLAND

[2]CLERMONT UNIVERSITE, UNIVERSITE BLAISE PASCAL, LABORATOIRE MAGMAS ET VOLCANS, BP 10448, F-63000 CLERMONT-FERRAND, FRANCE

[3]CNRS, UMR 6524, LMV, F-63038 CLERMONT-FERRAND, FRANCE

[4]IRD, R 163, LMV, F-63038 CLERMONT-FERRAND, FRANCE

[5]DEPARTMENT OF EARTH AND PLANETARY SCIENCES, TOKYO INSTITUTE OF TECHNOLOGY, OOKAYAMA, MEGURO-KU, TOKYO 152-8551, JAPAN

[6]INSTITUTE OF GEOLOGY, UNIVERSITY OF WARSAW, 02-089 WARSAW, ŻWIRKI I WIGURY 93, POLAND

[7]INSTITUTE OF HYDROGEOLOGY AND ENGINEERING GEOLOGY, UNIVERSITY OF WARSAW, 02-089 WARSAW, ŻWIRKI I WIGURY 93, POLAND

[8]INSTITUTE OF MINERALOGY, TU BERGAKADEMIE FREIBERG, BRENNHAUSGASSE 14, D-09596 FREIBERG, GERMANY

[9]DEPARTMENT OF GEOCHEMISTRY, GZG OF GEORG-AUGUST-UNIVERSITY, 37077 GÖTTINGEN, GOLDSCHMIDTSTRASSE 1, GERMANY

[10]MASS SPECTROMETRY LABORATORY, INSTITUTE OF PHYSICS, MARIE CURIE-SKŁODOWSKA UNIVERSITY, 20-031 LUBLIN, POLAND

[11]LABORATOIRE MAGMAS ET VOLCANS; OPGC, CNRS, UNIVERSITÉ JEAN MONNET, 23, RUE DR PAUL MICHELON, 42023 SAINT-ETIENNE, FRANCE

[12]DEPARTMENT OF GEOLOGY, CENTRE OF ADVANCED STUDY, UNIVERSITY OF DELHI, DELHI-110007, INDIA

RECEIVED AUGUST 3, 2010; ACCEPTED OCTOBER 13, 2011
ADVANCE ACCESS PUBLICATION NOVEMBER 24, 2011

Growth and regrowth textures, trace element and oxygen isotope compositions, and water content or species have been studied in alkali feldspars from the late Archaean Closepet igneous bodies. Feldspar crystals grew from mixed magmas that are characterized by a high degree of homogenization. The 3D depiction of trace element distribution indicates that the crystallization process was followed by interaction with fluids. The magmatic system involved in feldspar formation shows non-linear dynamics. The interaction with fluids is also deterministic, but in contrast to magmatic crystallization, it shows an increasing persistency in element behaviour. The degree of persistency of the element activities in both processes has been calculated using the Hurst exponent. The recrystallization (regrowth)

Corresponding author. E-mail: e.slaby@uw.edu.pl

process induced by fluids proceeded along crystal fractures and cleavages, causing selective enrichment in large ion lithophile elements (light rare earth elements), Pb, Y, and in various water species. It did not change the feldspar oxygen isotope signature. In turn, the incorporation of hydrogen species into feldspar domains reduced Al–O^-–Al defect densities in the structure, decreasing their luminescence. Water speciation shows persistent behaviour during heating, the process being reversible at least up to 600°C. Carbonate crystals with a mantle isotope signature are associated with the re-equilibrated feldspar domains. The feldspar compositions, the abundance of water species in them and the refractory nature of the residuum after heating, the unchanged oxygen isotopes and the mantle signature of co-precipitated carbonates testify that the observed recrystallization has taken place at temperatures above 600°C with H_2O–CO_2 fertile, mantle-derived fluids. The paper draws special attention to some methodological aspects of the problem. The multi-method approach used here (major element, trace element and isotope geochemistry, infra-red, cathodoluminescence, 3D depiction of geochemical data and fractal statistics) may help to recognize and separate the various processes throughout the alteration history of the pluton.

KEY WORDS: *alkali feldspar; Archaean batholith; geochemistry; Hurst exponent; mantle-derived fluids; megacryst; metasomatism; 3D depiction; water in nominally anhydrous minerals*

INTRODUCTION

Archaean alkali feldspars have been analyzed to determine and to quantify recrystallization induced by high-temperature fluids. Our knowledge of fluid compositions in Archaean rocks is mainly restricted to crustal fluids, particularly lower crustal fluids (e.g. Hansen *et al.*, 1984, 1995; Touret, 2005; Hansen & Harlov, 2007, 2009; Santosh & Omori, 2008*a*, 2008*b*; Santosh *et al.*, 2009). Less is known about Archaean mantle-derived fluids (Shimizu *et al.*, 2001; Sarangi *et al.*, 2009). The present study focuses on the late Archaean Closepet batholith, South India, which has been the subject of a number of geological, petrological and geochemical studies (for a review, see Moyen *et al.*, 2001*a*) and where fluid-induced recrystallization processes have previously been recognized (Radhakrishna, 1958; Divakara Rao *et al.*, 1972). This huge batholith (400 km long by 25 km wide) was emplaced in a major active shear zone that may have penetrated deep into the mantle. The shear zone not only acted as a drain for magma emplacement, but also constituted a preferential path for mantle or crust fluid circulation.

Feldspar, a nominally anhydrous mineral, is sensitive to fluid metasomatism and consequently is able to record fluid-induced changes. The recrystallization processes are interpreted as mutual replacement reactions, causing element redistribution (Lagache & Weisbrod, 1977; Parsons, 1978; Słaby *et al.*, 1988; Słaby, 1992, 1994; Labotka *et al.*, 2004; Niedermeier *et al.*, 2009; Parsons & Lee, 2009; Parsons *et al.*, 2009; Plümper & Putnis, 2009), oxygen isotope exchange (Fiebig & Hoefs, 2002; Cole *et al.*, 2004; Labotka *et al.*, 2004; Banerjee *et al.*, 2007), and incorporation of incompatible water species (Nakano *et al.*, 2001; Johnson & Rossman, 2003, 2004). These reactions are characterized by certain features. They result in the appearance of new intracrystalline alteration microtextures (Parsons & Lee, 2009). Selective dissolution, as a result of differences in the reactant and product solubility, causes an increase in intracrystalline porosity (Putnis, 2002). Accompanying the dissolution–reprecipitation process, component replacement most probably proceeds through thin aqueous films and seems to affect trace elements more than major elements (Parsons & Lee, 2009; Parsons *et al.*, 2009). However, depending on the component's activity in the fluid, the feldspar can be completely replaced by new feldspar domains of different major element composition and structural ordering (Słaby *et al.*, 1988; Słaby, 1992, 1994; Niedermeier *et al.*, 2009) or by pseudomorphs composed of numerous phases (Putnis *et al.*, 2005, 2007; Niedermeier *et al.*, 2009; Plümper & Putnis, 2009). To identify and track the reaction progress, bulk crystal chemistry and imaging techniques [scanning electron microscopy (SEM), transmission electron microscopy (TEM)] are usually applied. Close attention is also paid to the textures and microtextures.

In the present study we extend the above investigations by applying a multi-method approach, with lesser attention paid to textures and microtextures. For the recognition of the replacement mechanism, we use cathodoluminescence (CL) instead of back-scattered electron (BSE) images. To identify the fluid composition, we concentrate predominantly on geochemical tools and methods of geochemical data processing. The data obtained include major element, trace element and isotope geochemistry as well as infra-red (IR) spectroscopy. Three-dimensional (3D) modelling (digital concentration–distribution models) combined with fractal statistics is used for the detection and description of subsequent changes in terms of element behaviour. Using the multi-method approach we focus on the detailed recognition of high-temperature magmatic and post-magmatic fluid-induced recrystallization processes.

GEOLOGICAL SETTING

Dharwar craton

The South Indian Dharwar craton is composed of the three classical lithologies of Archaean terranes (Chadwick *et al.*, 2000): (1) a tonalite–trondhjemite–granodiorite (TTG) gneissic basement called the 'Peninsular Gneisses' with an age between 3·3 and 2·7 Ga (e.g. (Meen *et al.*, 1992; Taylor *et al.*, 1984); (2) two groups of volcano-sedimentary greenstones: an older one with ages between

3·3 and 3·0 Ga, which occurs as large enclaves or screens in the Peninsular Gneisses, and a younger one (3·0–2·7 Ga) that lies unconformably on the TTG basement; (3) Late Archaean K-rich granitic intrusions that crosscut the older lithologies (Friend & Nutman, 1991; Subba Rao *et al.*, 1992; Jayananda *et al.*, 1995, 2000; Nutman *et al.*, 1996) emplaced between 2·6 and 2·5 Ga.

Closepet granite

The Closepet granite is a huge magmatic body that extends north–south over more than 400 km, and is typically about 20–30 km wide (Fig. 1). It has been emplaced into a network of vertical shear zones that separate the western and eastern parts of the Dharwar craton (Moyen, 2000). Although the magmatic body is complex, it can be schematically subdivided into three main components (Jayananda *et al.*, 1995; Moyen *et al.*, 2003), as follows.

(1) The most abundant facies consists of porphyritic monzogranites containing large (2–5 cm) K-feldspar megacrysts in a coarse-grained (3–5 mm) matrix. It frequently contains dark, elongated, centimetre- to decimetre-sized (up to 10 m) enclaves of clinopyroxene-bearing micromonzonite and monzonite (Fig. 2).
(2) The clinopyroxene-bearing micromonzonite or monzonite also occurs, more rarely, as dykes in anatectic granites (Fig. 1a). Like the enclaves, these are thought to be comagmatic with their monzogranitic host. Frequently, they show 'mixing structures' [where 'mixing' refers to the progressive process of blending two or more magmas together to form a uniform hybrid magma (Moyen *et al.*, 2001*a*)].
(3) Pink and grey, equigranular granites form irregular bodies and dykes injected into the porphyritic monzogranites, migmatites and Peninsular Gneisses. They show a complete gradation from gneiss to anatectic granite (Friend, 1984; Jayananda, 1988; Newton, 1990; Moyen *et al.*, 1997, 2001*a*, 2001 *b*).

The Closepet granitoids form a typical calc-alkaline suite, being Ba- and Sr-rich (1500 and 1200 ppm, respectively, at 60% SiO_2), and with strongly fractionated rare earth element (REE) patterns [$(La/Yb)_N = 100$]. These chemical features, associated with relatively high Mg-number (0·50), are those of typical sanukitoids (high-Mg granitoids) (Shirey & Hanson, 1984; Stern *et al.*, 1989). In addition, because of their relatively high TiO_2 contents, they belong to the high-Ti sanukitoid suite (Martin *et al.*, 2010).

The low SiO_2 content of the less differentiated monzonites (50–55% SiO_2) precludes their derivation by partial melting of the surrounding Peninsular Gneisses (70% SiO_2). On the basis of major element, trace element and isotope geochemistry, Moyen *et al.* (1997, 2001*a*) showed that the whole range of compositions in the Closepet granite can be accounted for by mixing of a mantle-derived magma (clinopyroxene-bearing monzonite) with crustal melts generated by anatexis of the Peninsular Gneisses (pink and grey, equigranular granites). This conclusion is supported by field and petrographic evidence for mixing. Moyen *et al.* (2001*a*) also indicated that the mantle source had to be enriched, which is consistent with the presence of syn-plutonic lamprophyre dykes (Jayananda *et al.*, 2009). Those workers proposed that, as for other sanukitoids (Rapp *et al.*, 2006; Moyen, 2009; Martin *et al.*, 2010), the mantle might have been enriched by felsic melts of TTG composition. After partial melting of subducted basalt, the TTG melts percolated upwards into the mantle wedge where they were totally consumed by reaction with the peridotites; subsequent partial melting gave rise to Closepet-like, high-Ti sanukitoids.

Geochemical modelling (Moyen *et al.*, 2001*a*) showed that during emplacement the magma experienced two major events: (1) at depth it underwent limited (<10%) fractional crystallization of biotite and amphibole; the magmas were hydrous enough to delay plagioclase crystallization; (2) the hot magmatic intrusion induced partial melting of the surrounding 3·2 Ga gneissic crust, generating anatectic granites. The differentiated mantle-derived magma and the crustal melts mixed together, giving rise to a wide compositional range of magmas.

The southern Closepet granite has been dated with consistent results: 2·518 ± 0·005 Ga (zircon single grain evaporation; Jayananda *et al.*, 1995) 2·513 ± 0·005 Ga [sensitive high-resolution ion microprobe (SHRIMP) on zircon; Friend & Nutman, 1991]; 2·535 Ga (concordia ages on zircons; Buhl, 1987); and 2·530 Ga (U–Pb on allanite; Grew & Manton, 1984). In the north, only one age is available: 2·566 ± 0·030 Ga (SHRIMP on zircon; Nutman *et al.*, 1996) north of the Sandur Schist Belt. Moyen *et al.* (2003) argued that the small age difference may be related to slower cooling of magmas in the deep granulitic crust.

Fluid-induced processes in the Closepet magmatic body, documented by K-feldspar replacement of plagioclase and biotite of amphibole, have been recognized by Radhakrishna (1958) and Divakara Rao *et al.* (1972). In its southern part, the batholith is locally affected by fluid-induced charnockitization. The transition is well exposed in the famous Kabbaldurga quarry, where patches of charnockite overprint the granitic structures. Stähle *et al.* (1987) argued that the local development of charnockitization results from infiltration of carbonic fluids along ductile shears and foliation planes. Srikantappa *et al.* (1992) demonstrated that charnockitization is caused by fluids expelled from underlying massive charnockites.

Replacement textures, as well as the invasive development of charnockites and the fact that these structures obliterate the granite fabric, demonstrate that they developed through fluid circulation that took place late in the history of the granite, after crystallization ceased.

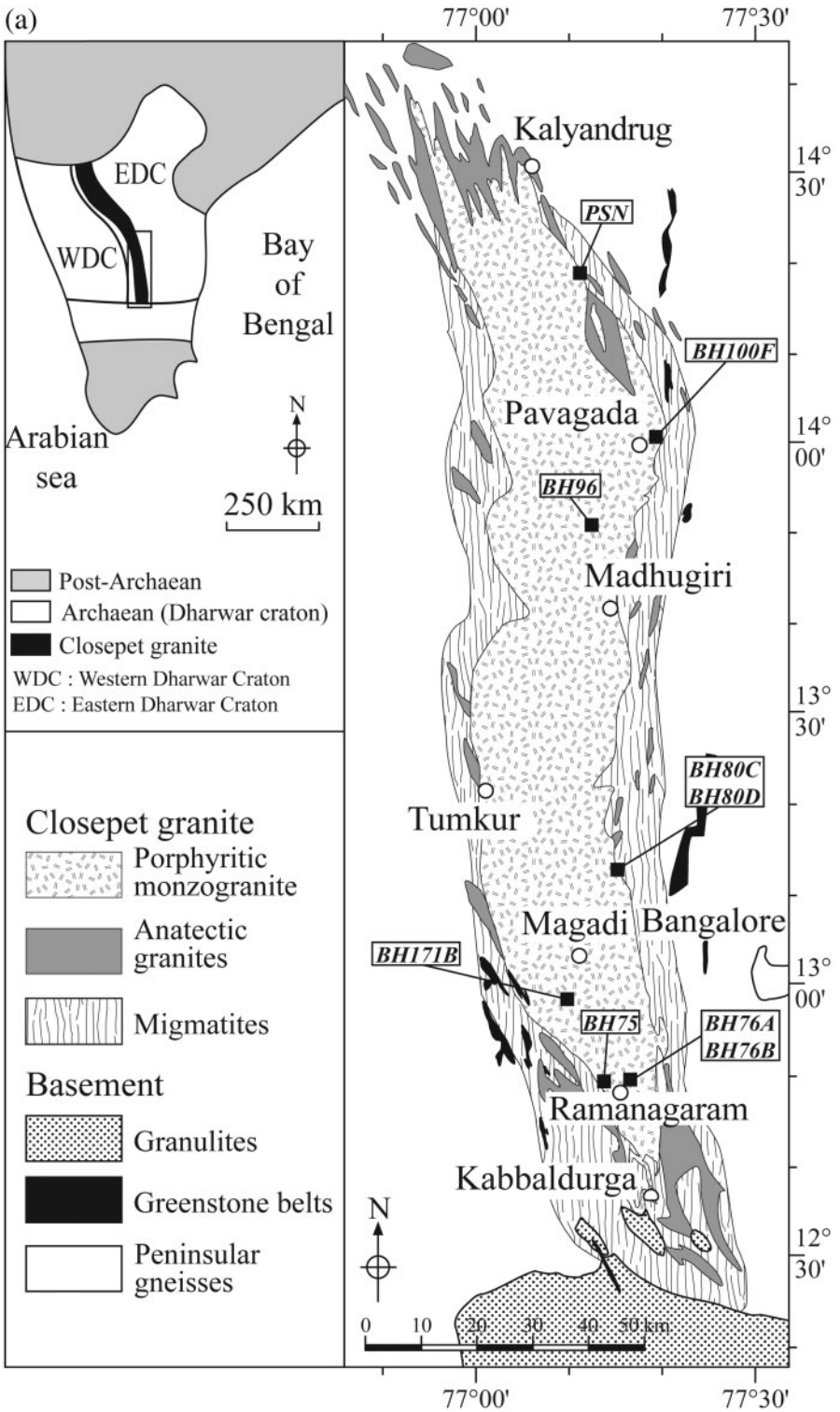

Fig. 1. (a) Schematic geological map of the southern part of the Closepet batholith, showing the sampling localities. (b) Sample localities corresponding to their vertical position in the batholith, giving an impression of their different emplacement conditions.

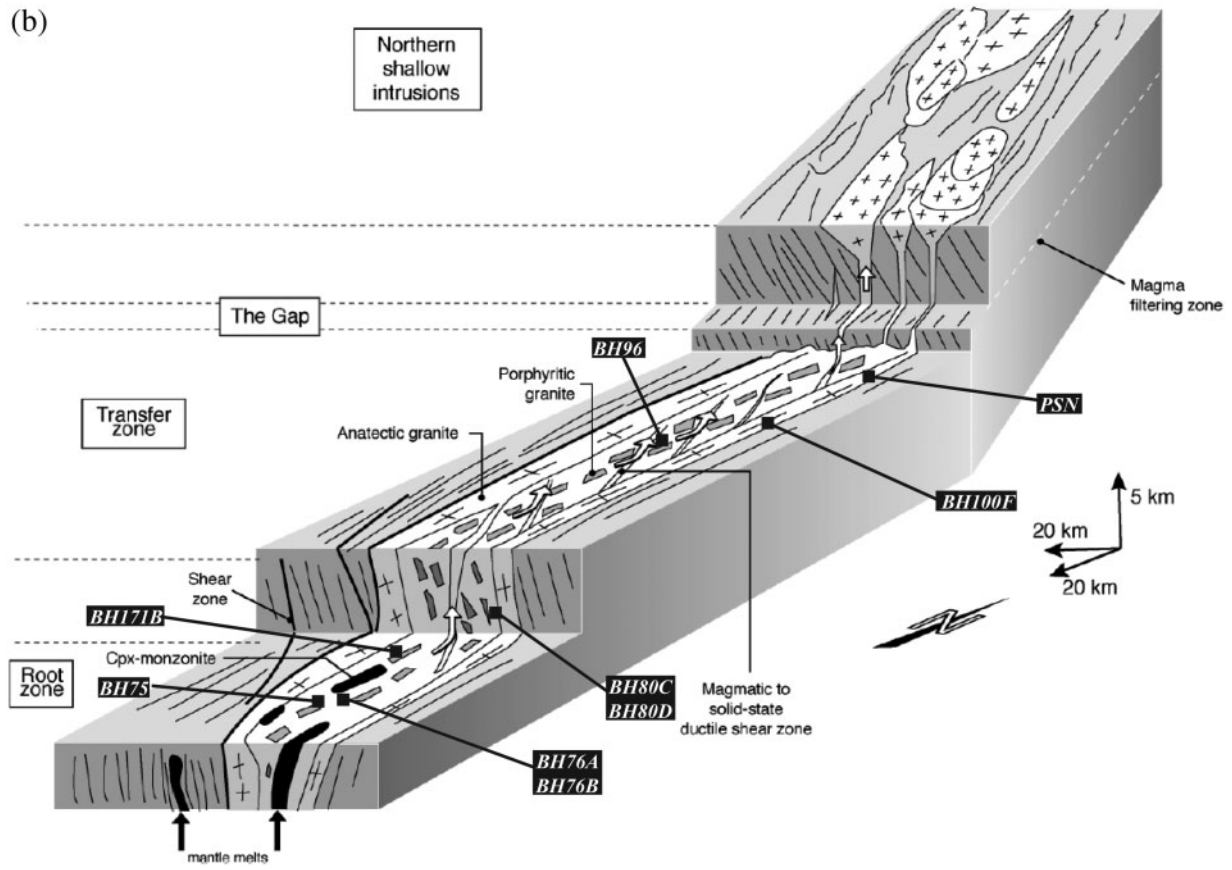

Fig. 1. Continued.

SAMPLE SELECTION

On the basis of petrographic observations of fluid-induced recrystallization of the batholith, fresh samples of the porphyritic monzogranite (BH75, BH76B, PNS, BH19A, BH80C, BH80D, BH96, BH171B) and one enclave sample comagmatic with its monzogranitic host (BH76A) without any visible shallow, meteoric alteration were selected for analysis (Fig. 1, Table 1). Most of the samples are located along marginal parts of the batholith, although two of them (BH96 and BH171) originate from the central part. The freshness of the samples was confirmed by microscopic, thin section observations.

Most of the samples are foliated, characterized by the alignment of feldspar megacrysts, and have a coarse-grained texture. The samples cover a wide range in composition ($60{\cdot}44\% \leq SiO_2 \leq 72{\cdot}53\%$) reflecting a wide range of differentiation (Table 2). All samples, except one, are alkali feldspar-bearing and considered to result from different degrees of mixing between two magmas (Moyen *et al.*, 2001*a*). One sample (BH100F) is silica-poor ($SiO_2 = 56{\cdot}92\%$) and contains no alkali feldspar, but instead contains plagioclase megacrysts. Moyen *et al.* (2001*a*) considered this as a cumulate generated by fractional crystallization of a mantle-derived parent magma.

Although granite emplacement proceeded under different P–T conditions (Fig. 1b) from south to north (Moyen *et al.*, 2001*b*), all the studied samples have similar mineral assemblages; they differ only in the relative abundances of minerals, growth textures and compositions (Table 1). The monzogranite contains patchy (pink–white or pink–translucent) anhedral to subhedral alkali feldspar megacrysts. Rapakivi textures are uncommon. The megacrysts are frequently surrounded by layers of highly strained groundmass composed of quartz and feldspar. The sheared matrix surrounds areas of coarse-grained, randomly oriented, equigranular matrix composed of subhedral plagioclase, amphibole and biotite, anhedral alkali feldspar and quartz. Single pyroxene relics, mantled by amphibole, occur in some of the monzogranites. As accessory minerals, apatite and zircon are common, whereas allanite, titanite, magnetite, ilmenite and monazite are less frequent. During shearing, the megacrysts

Fig. 2. Porphyritic granite and enclave, both containing alkali feldspar megacrysts (Toranagallu, Karnataka, India). Alkali feldspar megacrysts are composed of milky and translucent domains and are strongly cracked. The cracks, as well as surrounding domains, are turbid, and of orange–pink colour in hand specimen. Coin diameter 2·6 cm.

were cleaved and healed by carbonate crystals. In amphibole and biotite a few chlorite aggregates and plates are noticeable. Some of the accessory minerals show resorption textures and newly crystallized inclusions [among others light REE (LREE)- and Th-rich], which are probably the products of interaction with fluids.

The enclave sample (BH76A) is characterized by a predominance of dark minerals and consists of a fine- to medium-grained, mostly randomly oriented, assemblage of subhedral plagioclase and biotite, variable amounts of subhedral hornblende, subordinate quartz (partly mantled by mafic minerals), alkali feldspar and accessory titanite, apatite, ilmenite, magnetite and zircon. As in the porphyritic monzonite, single pyroxene relics mantled by amphibole and single alkali feldspar megacrysts, rarely with narrow rapakivi rims, are observed in the enclave. Their marginal parts show zones bounded by inclusion trails. In sample BH100F the dominance of dark minerals finds its strongest expression, biotite prevails over amphibole, and instead of alkali feldspar, plagioclase megacrysts appear.

The samples represent different stages of magmatic differentiation (Table 2). Simple correlations between the P–T conditions of magma emplacement, location within the batholith (Fig. 1b) and magmatic differentiation are, however, lacking. Samples from the southern part of the batholith are less differentiated (BH75, BH76B) and have been formed at higher P–T conditions (700°C and 6–7 kbar; Moyen *et al.*, 2003) than the least differentiated sample (BH100F) in the northern part, which was emplaced at 550°C and 5 kbar (Moyen *et al.*, 2003). The most differentiated samples BH171 (southern part) and BH96 (northern part) do not show any correlation with emplacement conditions.

Previous geochemical studies favouring mixing in the petrogenesis of the magmas (Jayananda *et al.*, 1992, 1995; Moyen *et al.*, 1997, 2001*a*) show excellent correlations in binary diagrams for most major elements (except alkalis) and some selected trace elements. Our data (Table 2) confirm these previously observed trends, but also show a significant number of trace elements with significant deviations from a linear trend; for example, Ba, LREE, high field strength elements (HFSE), Pb and Cs (Fig. 3). Many of the trace elements that show scatter are incorporated into the feldspar structure. Consequently, if the behaviour of these elements appears to be controlled by mixing, they cannot be satisfactorily accounted for by simple two-component mixing. In other words, this argues in favour of mixing having been overprinted by another process, which seems to have strongly affected the whole batholith.

ANALYTICAL METHODS

Major and trace element geochemistry

K-feldspar megacrysts were profiled by electron microprobe analysis (EMPA) in 10–100 μm steps. Major elements (Na, Al, Si, K, Ca) and some trace elements (Ba, Fe, Mg, Sr) were determined. The analyses of megacrysts were performed at the Laboratoire Magmas et Volcans,

Table 1: Sample description, rock textures and qualitative modal composition

Sample no.	Sample description	Mylonitic texture	Randomly oriented	Equigranular matrix texture	Mineralogical composition							
					Qtz	Afs	Pl	Am (Px)	Bt (Chl)	Op	Acc	Cc
BH100F	Angular, very dark, cumulate enclave; matrix grain size 1 mm; plagioclase megacryst 7 mm		••	••	•	•	••	••	••	•	•	
BH75	Grey, porphyritic monzogranite (from an outcrop showing mingling relations between pink equigranular granite, cpx-bearing monzonite and porphyritic granodiorite); matrix grain size 1–3 mm; alkali feldspar megacryst 1·5–3 cm	••	••	••	•	•	••	••(•)	••	•	••	
BH76B	Porphyritic granodiorite with 'proto-shear zones' showing reorientation of Afs megacryst. Some of the shear zones are injected by late aplite or fine-grained granite; matrix grain size 1–2 mm; alkali feldspar megacryst 1·5–3 cm	••	••	••	••	•	••	••	••	•	••	
BH76A	Microgranular mafic enclave, fine grained, with Afs megacryst (probably being 'pushed' from the porphyritic granite into the enclave). The enclaves are elongated in the foliation of the granite BH76A; matrix grain size 1 mm; alkali feldspar megacryst 1·5 cm		••	••	•	••	••	••	••	•	••	•
PNS	Porphyritic monzogranite, with white Afs megacryst	••	•		••	••	••	•	••	•	•	•
BH80C	Porphyritic monzogranite, with white Afs megacryst, cut by fine-grained grey dykes; matrix grain size 4–8 mm; alkali feldspar megacryst 1–4 cm	••	•	•	••	••	••	•(•)	••(•)	•	••	•
BH80D	Porphyritic monzogranite; apparently corresponds to some kind of segregate between megacrysts and intermediate liquids (probably by filter pressing or mechanical segregation); matrix grain size 4–8 mm; alkali feldspar megacryst 1–4 cm	••	•	•	••	••	••	•	••(•)	•	••	•
BH96	Porphyritic granite; matrix grain size 4–8 mm; alkali feldspar megacryst 1–4 cm	••	••	••	••	••	••	•	••(•)	•	•	
BH171B	Porphyritic monzogranite in a very heterogeneous outcrop, showing a range of facies from 'pink' Afs megacryst-bearing granite (pink megacrysts, matrix white to pinkish) to a 'grey' Afs megacryst-bearing monzogranite (grey matrix and white Afs megacrysts); the sample was taken from the pink, more equigranular granite; matrix grain size 4–6 mm	••	•	•	••	••	••		••	•	•	

Qtz, quartz; Afs, alkali feldspar; Pl, plagioclase; Am, amphibole; Px, pyroxene; Bt, biotite; Chl, chlorite; Op, opaque minerals; Acc, accessory minerals; Cc, carbonate; •• significant amount; • subordinate amount.

Table 2: Major and trace element composition of studied Closepet batholith samples

Sample:	BH100F	BH76A	BH75	BH76B	PSN	BH80C	BH80D	BH96	BH171B
Longitude:	77°17′26	77°16′68	77°15′22	77°16′68	77°12′14	77°17′16	77°17′16	77°12′18	77°10′63
Latitude:	14°06′64	12°44′34	12°44′06	12°44′34	14°16′11	13°10′94	13°10′94	13°53′51	12°59′29
SiO_2	56·92	60·44	60·96	61·41	65·33	65·68	66·8	70·15	72·53
Al_2O_3	12·90	16·61	16·95	16·16	14·67	15·78	15·24	15·02	14·44
Fe_2O_3	9·25	6·66	5·71	6·27	5·44	4·63	3·42	2·49	1·81
MnO	0·15	0·09	0·07	0·09	0·09	0·08	0·07	0·04	0·02
MgO	6·43	1·91	1·68	2·00	1·49	1·31	0·9	0·55	0·39
CaO	4·90	4·09	3·64	3·49	2·77	3·32	2·59	1·72	1·43
Na_2O	2·63	4·65	4·23	3·92	3·52	4·45	3·43	4·09	3·84
K_2O	4·37	3·34	4·73	4·45	4·87	3·22	5·97	4·82	4·51
TiO_2	0·79	0·91	0·76	0·83	0·65	0·63	0·59	0·33	0·26
P_2O_5	0·52	0·45	0·47	0·4	0·26	0·23	0·16	0·09	0·07
LOI	0·70	0·50	0·40	0·60	0·60	0·40	0·60	0·60	0·60
Sum	99·56	99·65	99·6	99·62	99·69	99·73	99·77	99·90	99·90
Cr	275	<10	<10	<10	14	<10	<10	34	<10
Sc	13	9	6	9	8	6	8	2	2
Ba	838	861	1352	1141	722	629	1169	659	672
Be	3	3	2	2	2	3	2	1	3
Co	36	15	12	14	11	11	8	5	3
Cs	2·4	0·3	0·6	0·5	2·1	2·3	1·1	0·4	0·8
Ga	16·8	20·1	19·5	19·9	19·2	20·1	18·5	18·4	17·5
Hf	6·5	8·2	8·2	8·6	9·8	7·2	10·1	6·6	5·7
Nb	14·1	17·8	10·1	13·7	20·6	18·3	31·7	9·0	6·5
Rb	185	81	126	113	162	128	152	167	137
Sr	722	886	1073	800	444	562	537	275	257
Ta	0·8	1·4	0·4	0·5	1·9	1·3	2·6	0·3	0·3
Th	12·7	8·3	14·3	10·5	38·7	15·8	24·8	30·5	13·3
U	2·1	0·6	0·7	0·8	3·4	1·3	3·9	1·4	1·3
V	105	108	83	92	68	65	51	26	19
Zr	274	288	316	314	331	250	357	227	192
Y	25	44	29	39	49	24	46	9	10
La	73	85	132	93	98	65	63	75	53
Ce	148	178	235	192	210	122	146	134	92
Pr	18	22	24	23	26	13	18	14	11
Nd	68	88	83	88	97	47	68	44	35
Sm	11	15	11	14	17	7·86	13	5·70	5·48
Eu	2·30	3·00	2·40	2·60	2·30	1·60	2·30	1·10	0·99
Gd	7·73	10·70	8·27	10·50	12·70	6·09	9·61	3·46	3·32
Tb	0·98	1·52	1·06	1·42	1·81	0·85	1·50	0·36	0·38
Dy	5·22	8·42	5·60	7·63	9·08	4·63	8·49	1·65	1·71
Ho	0·85	1·48	0·99	1·34	1·63	0·82	1·54	0·28	0·30
Er	2·30	3·94	2·45	3·61	4·45	2·13	4·26	0·85	0·76
Tm	0·34	0·66	0·39	0·55	0·72	0·34	0·72	0·14	0·12
Yb	2·11	3·84	2·14	3·35	4·22	2·11	4·24	0·98	0·77
Lu	0·29	0·50	0·30	0·46	0·56	0·30	0·58	0·14	0·11
Cu	59	40	25	25	19	39	37	4	7
Pb	9·5	4·9	4·1	5·0	17·7	8·2	13·0	14·0	7·6
Zn	84	86	78	78	69	83	44	52	40
Ni	154	10	9	13	11	10	9	3	2

LOI, loss on ignition.

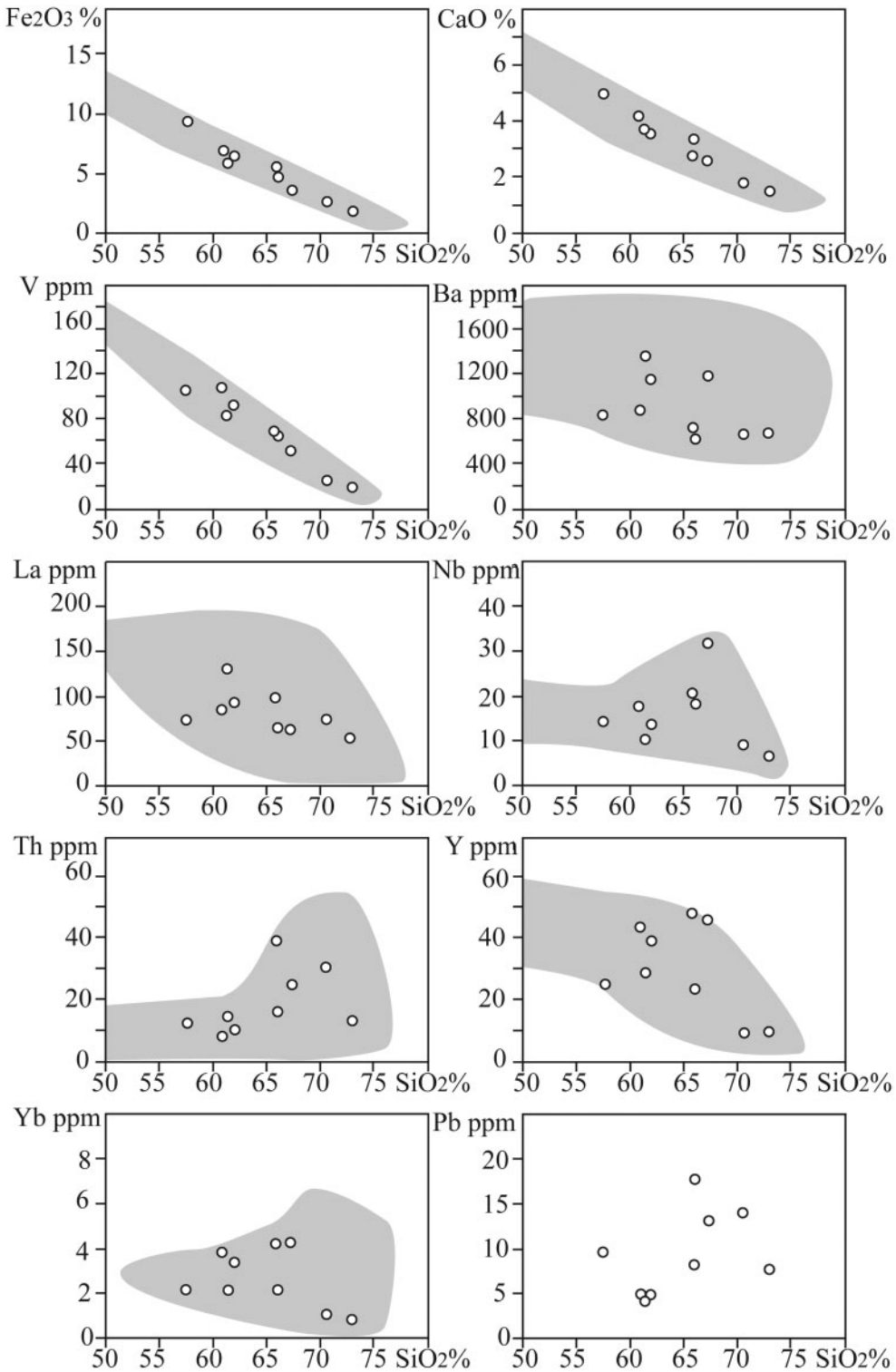

Fig. 3. Harker variation diagrams for the Closepet batholith samples. Linear correlations are observed between major and some trace element concentrations and silica content; data for other trace elements show scatter. Grey fields show data by Moyen (2000).

Clermont-Ferrand using a Cameca SX-100 electron microprobe with an accelerating voltage of 15 kV. Alkalis, Ca, Si and Al were analyzed first using a 15 nA beam current. Trace elements were analyzed at 50 nA. Counting times were 30 s for barium and Sr, 60 s for Fe and Mg, and 10 s for Al, Si, and Ca. Representative detection limits (3σ) for minor and trace elements were 220 ppm for Ba, 400 ppm for Sr, 200 ppm for Fe and 40 ppm for Mg.

Laser ablation inductively coupled plasma mass spectrometry (LA-ICP-MS) was carried out at the Geochemisches Institut, Göttingen University, using a Perkin Elmer DRC II instrument combined with a Compex 110 laser system @ ArF 193 nm (Lambda Physik, Göttingen) and a GeoLas optical system (MikroLas, Göttingen). The K-feldspar megacrysts were analysed along *c.* 1·5–2 cm transects by moving the laser spot at a constant speed of about 10–20 $\mu m\,s^{-1}$, 10 Hz repetition rate and 120 μm laser spot diameter over the thin section. The transect was repeated at a distance of about 2 mm several times to obtain a 2D image of the concentrations in the feldspar. Every 0·76 s there was a complete analysis of 30 isotopes: ^{23}Na, ^{24}Mg, ^{25}Mg, ^{27}Al, ^{29}Si, ^{31}P, ^{39}K, ^{43}Ca, ^{49}Ti, ^{55}Mn, ^{57}Fe, ^{85}Rb, ^{88}Sr, ^{89}Y, ^{96}Zr, ^{133}Cs, ^{137}Ba, ^{139}La, ^{140}Ce, ^{141}Pr, ^{143}Nd, ^{147}Sm, ^{151}Eu, ^{157}Gd, ^{163}Dy, ^{166}Er, ^{172}Yb, ^{208}Pb, ^{232}Th and ^{238}U. Spatial resolution is therefore about 20 μm. The laser line reached a depth of about 40 μm. Elemental concentrations were calculated using NBS610 for calibration and ^{29}Si as an internal standard.

Whole-rock compositions for major and trace elements were analysed at the ACME Analytical Laboratories, Vancouver (Canada) (for analytical procedures see http://acmelab.com). All analyses were recalculated on an anhydrous basis, with iron expressed as $Fe_2O_{3t} = Fe_2O_3 + 1{\cdot}111FeO$.

Isotope analysis

Oxygen isotope compositions were determined on thick sections of feldspar, using isotope ratio monitoring–gas chromatography–mass spectrometry (irm–GC–MS) with ArF laser fluorination. The analytical method has been described by Wiechert & Hoefs (1995), Wiechert *et al.* (2002) and Gao *et al.* (2006). The spatial resolution of the laser pits is around 350 μm. The average internal analytical precision is generally better than ±0·2‰, assessed by duplicate analysis of standards. The analysis of feldspars, however, represents a special problem, as feldspars can react with fluorine at room temperature before laser treatment, which may lower the precision of the oxygen isotope analysis. To reduce this effect, repeated fluorinations before UV-laser ablation were carried out; nevertheless, we assume that the precision in our study is not better than ±0·3‰. The δ-values are reported in the conventional δ-notation relative to VSMOW.

Carbon isotope analysis was performed in the Mass Spectrometry Laboratory at Marie Curie-Skłodowska University (Lublin, Poland) using a dual inlet and triple collector instrument. CO_2 was liberated from rocks containing carbonates by reaction with 100% phosphoric acid at 25°C for over 1 h. The δ-values were normalized to the VPDB scale using the NBS-19 calcite standard. Standard uncertainty (1σ) of the measured delta values did not exceed 0·06‰.

Spectroscopic analysis

CL microscopy and spectral CL measurements were used to document growth zoning and internal textures within the K-feldspar megacrysts and apatites. The CL measurements were made on carbon-coated, polished thin sections using a hot cathode CL microscope (HC1-LM (Neuser *et al.*, 1995) operated at 14 kV accelerating voltage and a current density of *c.* 10 $\mu A\ mm^{-2}$. Luminescence images were captured on-line with a Peltier-cooled digital video camera (KAPPA 961-1138 CF 20 DXC). CL spectra in the wavelength range 380–900 nm were recorded with an Acton Research SP-2356 digital triple-grating spectrograph with a Princeton Spec-10 CCD detector attached to the CL microscope by a silica-glass fiber guide. CL spectra were measured with wavelength calibration by a Hg-halogen lamp, a spot width of 30 μm and a measuring time of 2 s.

Trace amounts of water in nominally anhydrous minerals can be detected sensitively by IR spectroscopy. In this study, water in feldspar was analyzed by Fourier transform IR spectrometry (FTIR) using a Jasco-610 system at the Institute for Geothermal Sciences, Kyoto University. The spectrometer is equipped with a halogen lamp, CaF_2 beam splitter, CaF_2 polarizer, and N_2-cooled InSb detector. The spectra were collected with a resolution of $4\ cm^{-1}$ and consist of 128 scans. Water in feldspar megacrysts was analyzed using an unpolarized IR beam in a double-polished thin section. The obtained mid-IR band area of unpolarized IR beam per unit thickness was then converted to the hydrogen concentrations of feldspars measured by polarized IR spectroscopy, because the two are linearly correlated. The detailed procedure of this calibration is described below. High-temperature IR analyses were carried out on a Linkam 1500 heating stage. The stage temperature was controlled using a Linkam TMS93 unit.

DATA PROCESSING

Two methods of data processing have been combined to separate the effects of overlapping magmatic and post-magmatic processes: fractal statistics and 3D data depiction (Domonik *et al.*, 2010; Śmigielski *et al.*, 2011).

Fractal statistics

A fractal-based method—rescaled range analysis (R/S)—was used to detect the presence or absence of trends in time series (non-stationary signals, e.g. geochemical data series), by finding the Hurst exponent (Mandelbrot & Van Ness, 1968). The fractal dimension, D, can be derived from the Hurst exponent, H, by the relation $D = 2 - H$. The Hurst exponent (also called the roughness exponent; Feder, 1991) gives a measure of the smoothness of a fractal object where H varies between zero and unity, and helps to distinguish between random and non-random data patterns. In the present study H is calculated by Hurst's rescaled range analysis method (R/S) as improved by Peters (1994). For a given set of data $x_1, x_2, \ldots, x_n$ (e.g. selected LA-ICP-MS profiles), for n periods (number of sectors) and a sample mean, the classical rescaled range formula is expressed as follows:

$$R/S = \frac{1}{S}\left[\max_{1<k<n}\sum_{j=1}^{k}(xj - \bar{x}\bar{n}) - \min_{1<k<n}\sum_{j=1}^{k}(xj - \bar{x}\bar{n})\right]$$

where S is the standard deviation. The relationship between R/S and H can be expressed as $R/S = an^H$. The Hurst exponent can be estimated using the following regression: $\log(R/S) = \log(a) + H[\log(n)]$ and by plotting it, where $Y = \log(R/S)$ and $X = \log n$ and the exponent H is the slope of the regression line.

The self-similarity parameter, which is the Hurst exponent (H), shows the long-range dependence of element behaviour during the processes. The H value ranges between zero and unity; a value of 0·5 indicates a random distribution indistinguishable from noise. For values greater or less than 0·5, the system shows non-linear dynamics. $H < 0{\cdot}5$ represents anti-persistent (more chaotic) behaviour, whereas $H > 0{\cdot}5$ corresponds to increasing persistence (less chaotic). Such persistence is characterized as an effect of a long-term memory, and thus by a large degree of positive correlation. In theory, the preceding data constantly affect the next in the whole temporal series. In the language of probability, if in the past the process generated an increasing trend, there is a chance that this trend will be followed in the future; for example, for $H = 0{\cdot}8$ there is an 80% chance that this trend will be followed in the future. Applied to chaotic dynamics, the system shows a subtle sensitivity to the initial conditions. The process can show some degree of chaos, owing to local variations, but generally the trend preserves its persistent character through time. If $H < 0{\cdot}5$, the process shows frequent and sudden reversals. The trends appearing as a result of the progress of such a process show mutual negative correlation of the succeeding values in the data series. Low H values predict with a high probability that an increasing tendency in a trend in the past will imply change in the direction of the upcoming trend in the future. Thus, the system can be described as having a high degree of deterministic chaos. Holten *et al.* (1997), Turcotte (1997) and Hoskin (2000) have used the fractal approach to analyze self-affine processes in zoned minerals.

Three methods of data pre-selection have been tested to calculate the Hurst exponent: (1) all the LA-ICP-MS data collected along transects have been used; (2) to take into account the presence of alkali feldspar, all mineral inclusions have been removed based on potassium concentration; (3) the filter used for data pre-selection in the third test was the minimum Ba content in the alkali feldspar, indicative of crystallization from a crustal end-member magma. The assumed partition coefficient for Ba ($K^{Ba}_{afs/melt} = 11{\cdot}4$) was from Nash & Crecraft (1985). All filtering methods led to similar results. The pre-selection usually resulted in the loss of about 4% of the whole population of data along a single profile.

The 3D depiction of geochemical data

The 3D depiction of LA-ICP-MS data in contour maps and surface models of element distribution were set up with the use of Surfer 8.0 (Golden Software). Data pre-selection (see the section 'Fractal statistics' above) was carried out to exclude mineral inclusions in the megacrysts. After data selection, several grid resolution and interpolation methods were tested: minimum curvature, radial basis function, triangulation with linear interpolation and inverse distance to a power. Final interpolation was made using the kriging method with a grid resolution of 21×27 (Cressie, 1990). The applied grid resolution allowed us to overcome differences between data resolution along and across LA-ICP-MS profiles and to show the major trends of element distribution. After interpolation, models were spline smoothed (without recalculation) to a resolution of 287×221 to eliminate angular surfaces. Subsequently, maps of Hurst exponent values were interpolated using the same method in the same grid without spline smoothing. To calculate the maximum value of the gradient and its direction for surface models of element distribution the second-order finite-difference technique of Fleming & Hoffer (1979) was used. All maps of the gradient value were constructed retaining the same scale of surpass to allow comparison of the dynamics of the change of concentration. Plots of the direction of maximum gradient were constructed making averages of up to four sectors.

ALKALI FELDSPAR MEGACRYSTS STUDY—RESULTS AND DISCUSSION

Megacryst characteristics

Megacryst description

Alkali feldspar megacrysts are subhedral to anhedral, 1–4 cm in size, with two domains (Fig. 4a and d): (1) a

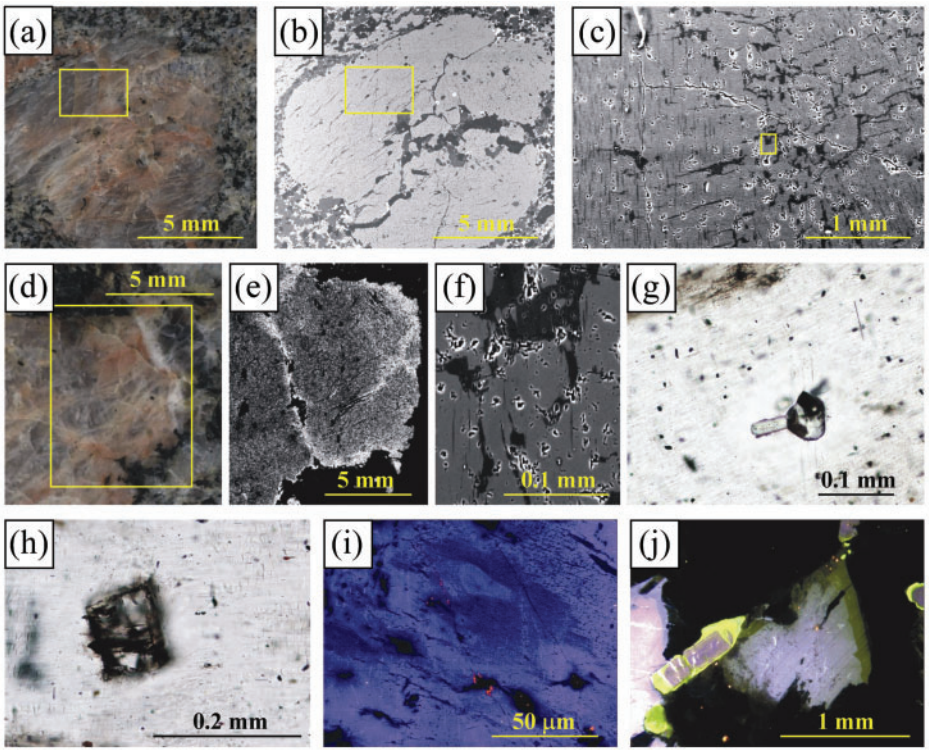

Fig. 4. Megacryst characteristics. (a) Monzogranite rock slab with alkali feldspar megacryst. The feldspar displays a typical growth morphology: a mixture of irregular water-clear and dusty pink domains (sample BH75; crystal length 1 cm). (b) BSE image of thin section from the slab. No differences between translucent and turbid domains are visible at this scale. The marked area is shown in (c) and (f). (c) The translucent domain (on the left) displays regular perthite structure, whereas the turbid area (on the right) is more porous and cracked. The rectangle outlines patch perthite shown in (f). Cracked and marginal parts of the crystal BH76A (d) are enriched in barium [(e) thin section map]. Translucent domains contain melt inclusions [(g) melt inclusion with accessory minerals, apatite and zircon; (h) melt inclusion with minute crystals of zircon], whereas dusty pink domains do not. Differences between translucent and pinkish domains are better visible under CL. (i) Fluid-induced textures—progressive changes in perthite texture. (j) Interface between magmatic and recrystallized marginal part in plagioclase (on the right), apatite (in the middle) and alkali feldspar (on the left).

transparent, colourless domain; (2) an opaque and white domain or a turbid, dusty pink and always opaque domain. The dusty type is widespread along rims, and cracks within crystals. All megacrysts are rich in mineral inclusions, mostly plagioclase, which are randomly distributed or spread into trails. The marginal parts of the megacrysts are rich in biotite, quartz and accessory minerals. Carbonates are associated with the turbid megacryst domains and generally do not occur in the transparent domains.

Transparent and turbid domains—BSE and CL images

BSE images show differences between the turbid and transparent megacryst domains (Fig. 4a and b). The observed textures are similar to those observed by Putnis *et al.* (2007) and Parsons & Lee (2009). The turbidity or 'milkiness' is commonly considered as evidence for increasing feldspar porosity owing to fluid interaction (Putnis, 2009). The 'pinkish' look is probably due to iron oxides in nano-pores in the turbid areas (Putnis *et al.*, 2007). Indeed, the turbidity in the investigated feldspars is associated with the more porous and cracked crystal parts (Fig. 4c). Fluid-induced coarsening of feldspar exsolution results in patch perthite that is observed in some parts of the domains (Fig. 4f), whereas clear domains show regular perthite exsolution. The early stages of coarsening are more easily visible under CL than in BSE images (Fig. 4i) (see also Parsons & Lee, 2009). In BSE images clear interfaces and a sharp reaction front are visible between patch perthite and the host crystal, but are not visible between the turbid and translucent domains. In contrast, the sharp reaction front in minerals is easily visible under CL (Fig. 4j). The recrystallization process changes the defect density in the structure in both domains. The translucent domains display light blue luminescence (higher structural defect density), whereas the dusty pink domains exhibit dark blue luminescence (reduced defect density).

All K-feldspar megacrysts display a bluish CL colour (Fig. 5), which is sometimes slightly patchy (Fig. 5a).

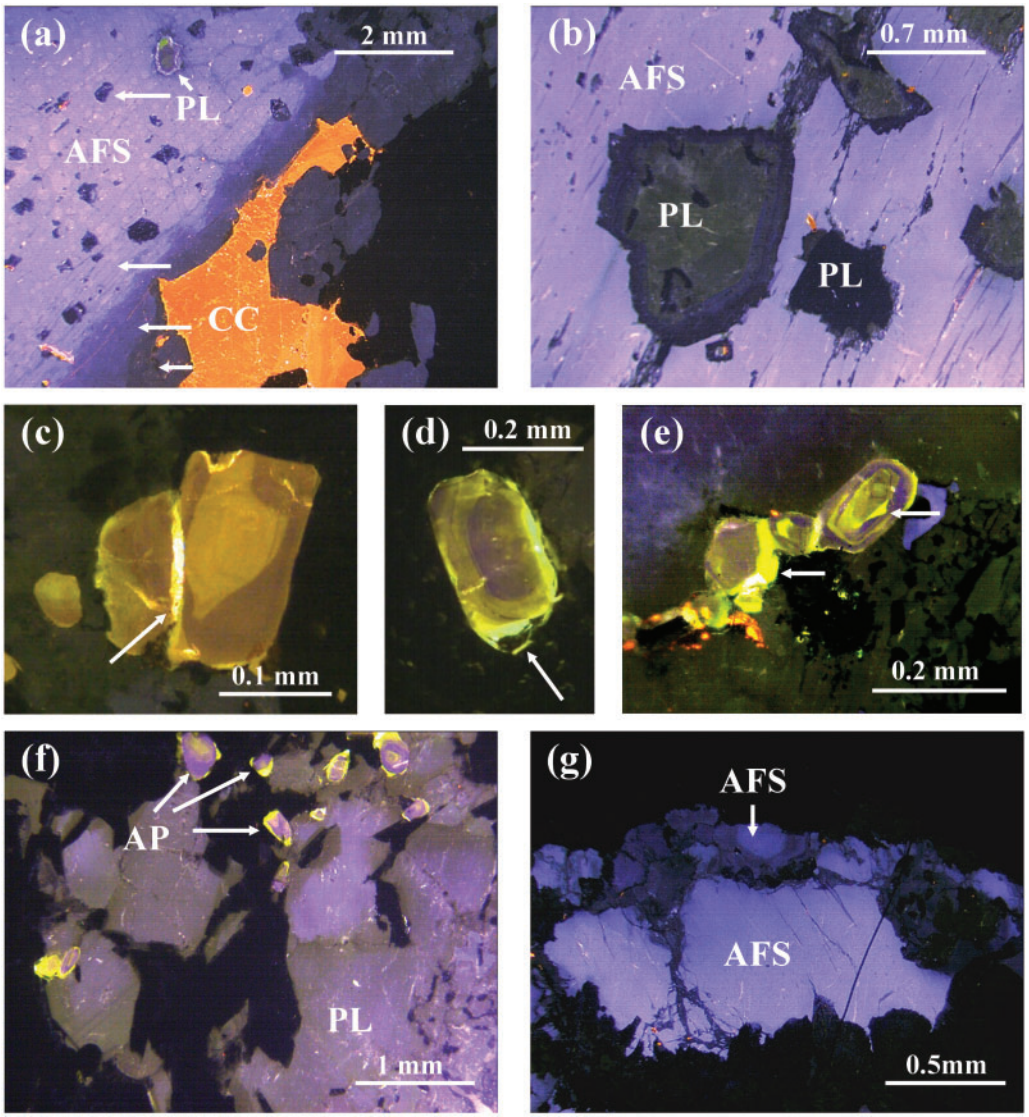

Fig. 5. CL micrographs showing growth and regrowth textures of feldspars and apatite. AFS, alkali feldspar; PL, plagioclase; CC, carbonate; AP, apatite. (a) Marginal part of an alkali feldspar megacryst (sample 80C); there is a progressive change in intensity of the blue CL colour from dark to medium and light (arrows); the reaction causing the appearance of dark blue luminescence implies simultaneous carbonate crystallization; reaction rims (short arrow) are also visible on plagioclase inclusions. (b) Plagioclase inclusions with reaction rims within an alkali feldspar megacryst (sample 80D); margins of plagioclase show at least two reaction zones; between two plagioclase inclusions a path of probable element migration is clearly visible. (c–e) Zoned apatite crystals with primary growth zoning, pointing to a multiple change in growth conditions during the crystallization of apatite in the magma. (f) Zoned apatite and matrix plagioclase with patchy marginal zones (sample 19A); the apatite crystals show pale yellow luminescent rims, which result from hydrothermal overprinting (arrows). (g) Matrix alkali feldspar (sample 19A), the marginal part as well as cracks in the crystal show dark blue luminescence.

The marginal part of the megacrysts frequently reveals a dark blue colour, which gradually changes to light blue (Fig. 5a). Measurements reveal that the spectra consist of two main emission bands that are caused by variable densities of Al–O^-–Al structural defects (~450 nm; blue) and by differing concentrations of Fe^{3+} activators (~700 nm red CL emission) (Marfunin & Bershov, 1970; Finch & Klein, 1999; Götze *et al.*, 2000). Dark blue luminescence is caused by a considerably reduced density of Al–O^-–Al structural defects (Fig. 6a). The megacrysts are also variably cracked (see for comparison Fig. 2); the cracks show dark blue luminescence.

The cracks and the dark blue marginal parts of the megacrysts are accompanied by tiny carbonate crystals (Fig. 5a–e; patches of bright orange–red luminescence). Plagioclase inclusions, frequently connected by cracks, in the megacrysts show broad, zoned reaction rims (Fig. 5b) with very dark blue luminescence. The intensity of

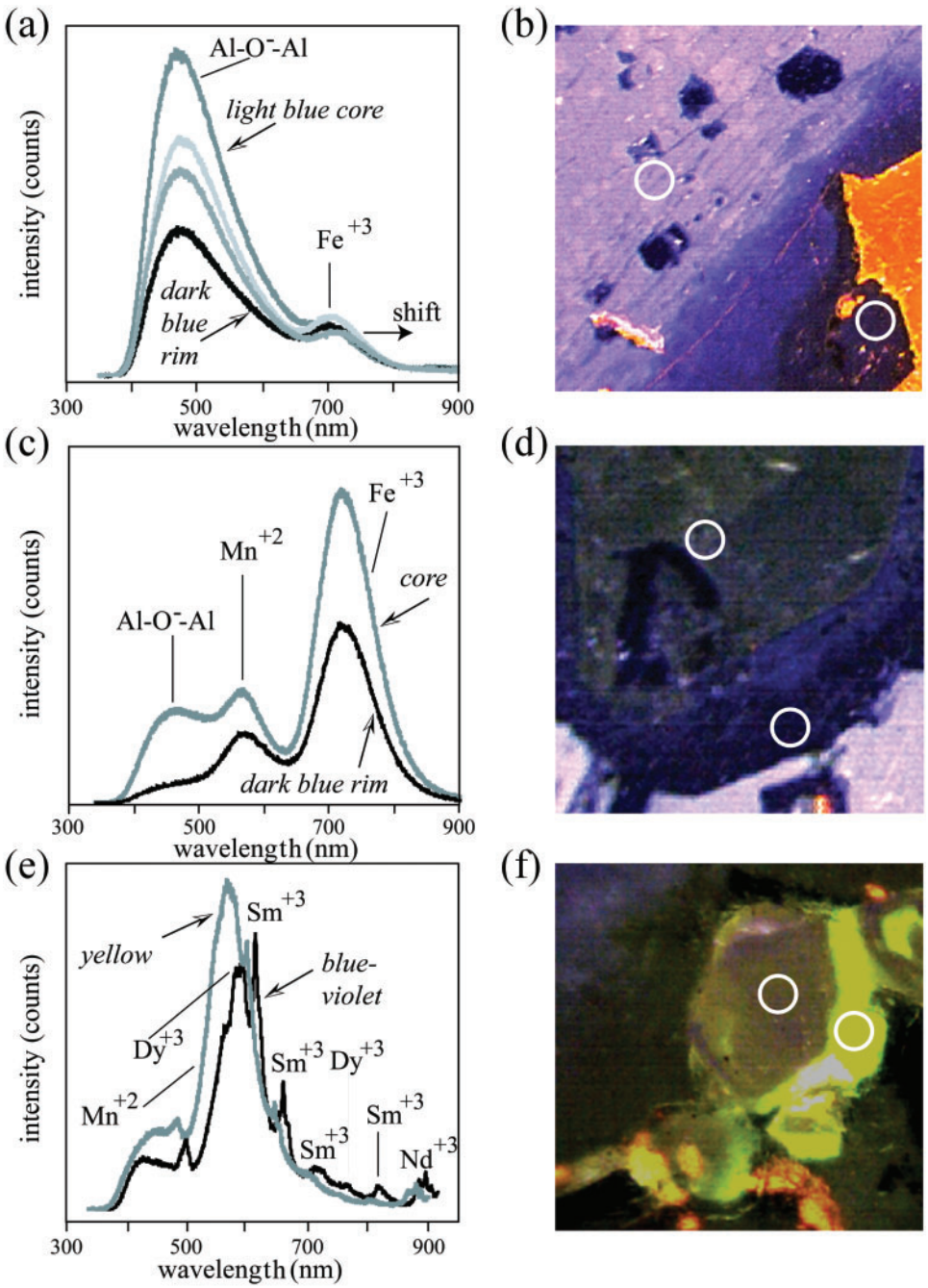

Fig. 6. CL images with analytical points (circles) and related spectra of pristine areas and domains changed as a result of recrystallization in crystals of alkali feldspar (a, b), plagioclase inclusion (c, d) and apatite (e, f) (compare with Fig. 8a, b and e). It should be noted that re-equilibrated marginal parts of feldspars show lower densities of Al–O$^-$–Al defects. The process also causes a shift of the ~700 nm red emission in alkali feldspar. The chemistry of the marginal part (yellow emission with a dominant band at ~575 nm owing to Mn^{2+}) of apatite is considerably changed in comparison with the core (blue–violet emission owing to dominant REE activation).

luminescence increases from the darkest outer reaction zone to a more bluish zone that changes into a blue–brown luminescent core activated by Mn^{2+} and Fe^{3+} (Fig. 6b). The CL spectrum collected within the alteration zone shows a considerable reduction in the density of Al–O$^-$–Al structural defects (450 nm emission). The change in the intensity of the bluish colour is also visible in the matrix alkali feldspar and plagioclase (Figs 4j, 5f and g). Their marginal parts show irregular, patchy patterns.

The CL spectra (Fig. 6a and b) illustrate that the dark blue parts of the K-feldspar megacrysts show low intensities of the blue emission band at *c.* 450 nm (Al–O^-–Al centre). A similar effect was observed by Finch & Klein (1999) and related to an interaction with fluids. Lowering of the defect density by recrystallization (ordering of the crystal lattice and healing of defects) has been reported by Van den Kerkhof & Hein (2001) and Van den Kerkhof *et al.* (2004) for trails in quartz, which have been affected by secondary fluid migration. Similarly, the studied fluid-induced textures appear to be visible owing to different densities of structural defects (Figs 4i, j, 5a, b, f, g and 6a–d). Thus the replacement reaction is connected to structural transformation (i.e. changes in structural ordering).

The reaction with fluids is also visible in apatite, where multiple CL growth zoning (Fig. 5d–f) points to a multiple change in growth conditions during crystallization from mingled magmas. However, the magmatic growth textures are overprinted by a second process mostly providing Mn to the apatite structure, which activates bright yellow CL (Fig. 6e and f). Generally, the outer zones are marked by this bright yellow luminescence, but also some inner zones (Fig. 5e) and all cracks within apatite crystals. The altered parts of the apatite have increased contents of Cl and F (Fig. 7).

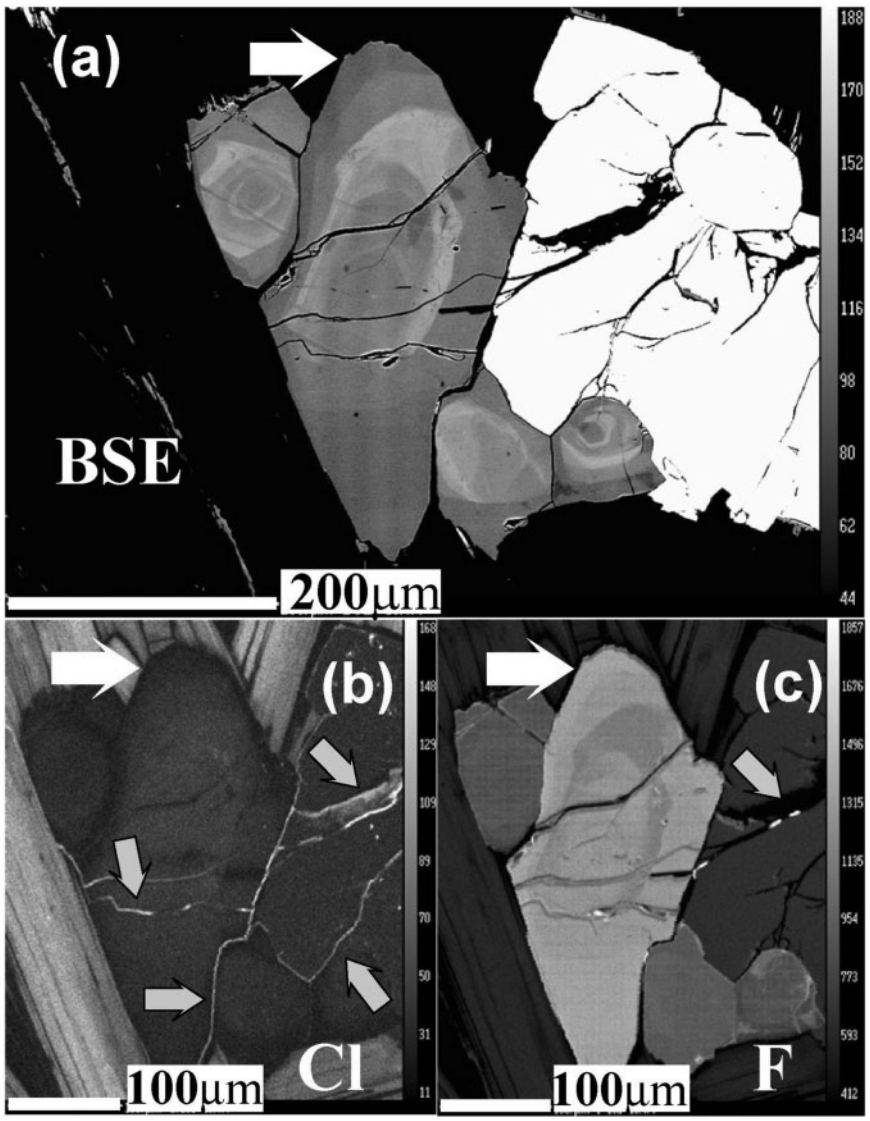

Fig. 7. Apatite crystals from sample 80C. Complex magmatic zoning resulting from two end-member magma mixing is cut by an external zone that formed as a result of fluid–crystal reaction (a). The crystal part grown from the mixed magma shows homogeneous Cl distribution and its depletion in external zones; in turn, some intragranular fractures in apatite and adjacent crystals show considerable Cl enrichment (b); the external zone is F-rich (c).

Textures observed in megacrysts, matrix feldspars and in apatite point to exchange with the migrating fluids, which resulted in gradual variations of CL from the margin to the core of the crystals (Figs 4j, 5 and 6). Dark luminescent cracks in both megacryst and matrix feldspar and light yellow luminescent cracks in apatite denote the fluid paths.

Domain compositions—EMPA profiles

The chemical composition (major and trace element) of the megacrysts was determined based on traverses along a single line (Supplementary Data Table 1, available for downloading at http://www.petrology.oxfordjournals.org). The major element compositions indicate that they are K–Na feldspar solid solutions ranging from $Or_{67}Ab_{33}An_0$ to $Or_{98}Ab_2An_0$ (average $Or_{83}Ab_{17}An_0$). Barium, a slowly diffusing compatible trace element (Cherniak, 2002), was used to track, step-by-step, the K-feldspar growth histories. The trace element traverses (Fig. 8a) are arranged according to increasing magmatic differentiation, from the sample with lowest (BH75) to that with highest silica content (BH96–BH171B).

All the K-feldspar megacrysts display similar Ba distribution patterns with a compositional plateau (translucent domains) where the Ba content is almost constant throughout the megacryst. The regularity of this plateau undergoes local perturbations (turbid domains). The 'plateau' concentration seems to change with progressive magmatic differentiation from 4500 ppm (BH75) to 1500 ppm (BH96) and can be ascribed neither to fractional crystallization nor magma mixing acting alone. In addition, all the megacryst profiles lack a regular zoned pattern, which is common for feldspars grown from mixed magmas (Vernon, 1986; Gagnevin *et al.*, 2005*a*, 2005*b*; Słaby *et al.*, 2007, 2008; Vernon & Paterson, 2008). The Ba concentration pattern may point to crystallization in an environment with a high degree of homogenization (blending); that is, a magma with only local, small heterogeneity. Single, irregularly occurring, narrow peaks of high Ba concentration might be relicts of active magma regions, enriched in mantle-derived (Ba-rich) components [i.e. poorly mixed in the sense of Perugini *et al.* (2002)]; however, other observations argue against this hypothesis.

The binary Ab–Or composition points to variably exsolved sodic orthoclase (Fig. 8b). Alkali incorporation into feldspar is temperature-dependent, with increasing Na preference with increasing temperature. Moyen *et al.* (2001*a*) demonstrated that the Closepet granite resulted from mixing of two thermally and compositionally different magmas, a mantle-derived magma with 1650 ppm Ba, and a crustal-derived one with 650 ppm Ba. The composition of the feldspar, fed during its growth by the active magma regions, should result in simultaneous Na and Ba enrichment; however, the Ba-rich domains in the feldspar display the opposite tendency. They are almost pure orthoclase (Fig. 8b). Barium EMPA mapping (Fig. 4e) documents Ba enrichment only along some marginal parts of the megacrysts or along cracks, which cannot be explained by mixing or any other magmatic process. The magmatic origin of the translucent domains is confirmed by the presence of melt inclusions containing tiny grains of accessory minerals (J. Touret, personal communication) (Fig. 4g and h). These are absent in the turbid areas.

Plagioclase inclusions incorporated into the K-feldspar megacrysts have a wide compositional range, which supports their crystallization from mingled magmas (Supplementary Data Table 1). They show narrow marginal rims of almost pure albite, which cannot be attributed to magmatic crystallization (compare Figs 5b and 6c and d). Calcium removed from plagioclase may have been incorporated *in situ* into carbonates, which accompany the Ba-enriched domains in the alkali feldspars.

Isotope studies

The oxygen isotopic composition of the feldspar megacrysts has been determined in both the transparent and dusty pink domains (Table 3) to constrain the nature of feldspar–fluid interaction. Measurements were made on two samples, the least and the most differentiated (BH75 and BH171B). The $\delta^{18}O$ values for both domains are within analytical uncertainty ($7{\cdot}49 \pm 0{\cdot}1$‰ and $7{\cdot}34 \pm 0{\cdot}3$‰ respectively) and are very close to those measured on different domains in plagioclase ($7{\cdot}49 \pm 0{\cdot}2$‰) by Blancher (2004) from the Closepet granite. The $\delta^{18}O$ of the whole-rock varies from 6 to 8·5‰ (Blancher, 2004), values typical of I-type granites (Chappell & White, 1974) and the 'normal' group of Taylor (1978).

The carbon and oxygen isotope compositions of carbonates are summarized in Table 3. Carbon isotopes are very homogeneous ($\delta^{13}C$ V-PDB $= -5{\cdot}13 \pm 0{\cdot}5$‰), which is usual for oxygen isotopes ($\delta^{18}O$ VSMOW $= 9{\cdot}16 \pm 0{\cdot}6$‰), although three samples (BH76a, BH76b and BH171B) deviate from the average value.

Both the transparent and the dusty pink domains (Table 3) are isotopically homogeneous. In the case of late re-equilibration with hydrothermal fluids, higher $\delta^{18}O$ values would be expected (Fiebig & Hoefs, 2002; Cole *et al.*, 2004; Banerjee *et al.*, 2007). Consequently, the fact that the altered feldspar domains remain unchanged in $\delta^{18}O$ indicates high-temperature interactions with fluids derived from the mantle or from the lower crust. The estimated temperature of quartz–plagioclase pairs based on $\delta^{18}O$ ranges from 750 to 900°C (Blancher, 2004), which can be taken as a rough temperature estimate for the formation of the turbid and translucent domains in the megacrysts. High-temperature oxygen isotope exchange is generally coupled with cation exchange in feldspar, both being strongly correlated (Labotka *et al.*, 2004). Oxygen diffusivity in alkali feldspar is of the same order of magnitude as alkalis or slightly higher (Brady & Yund, 1983;

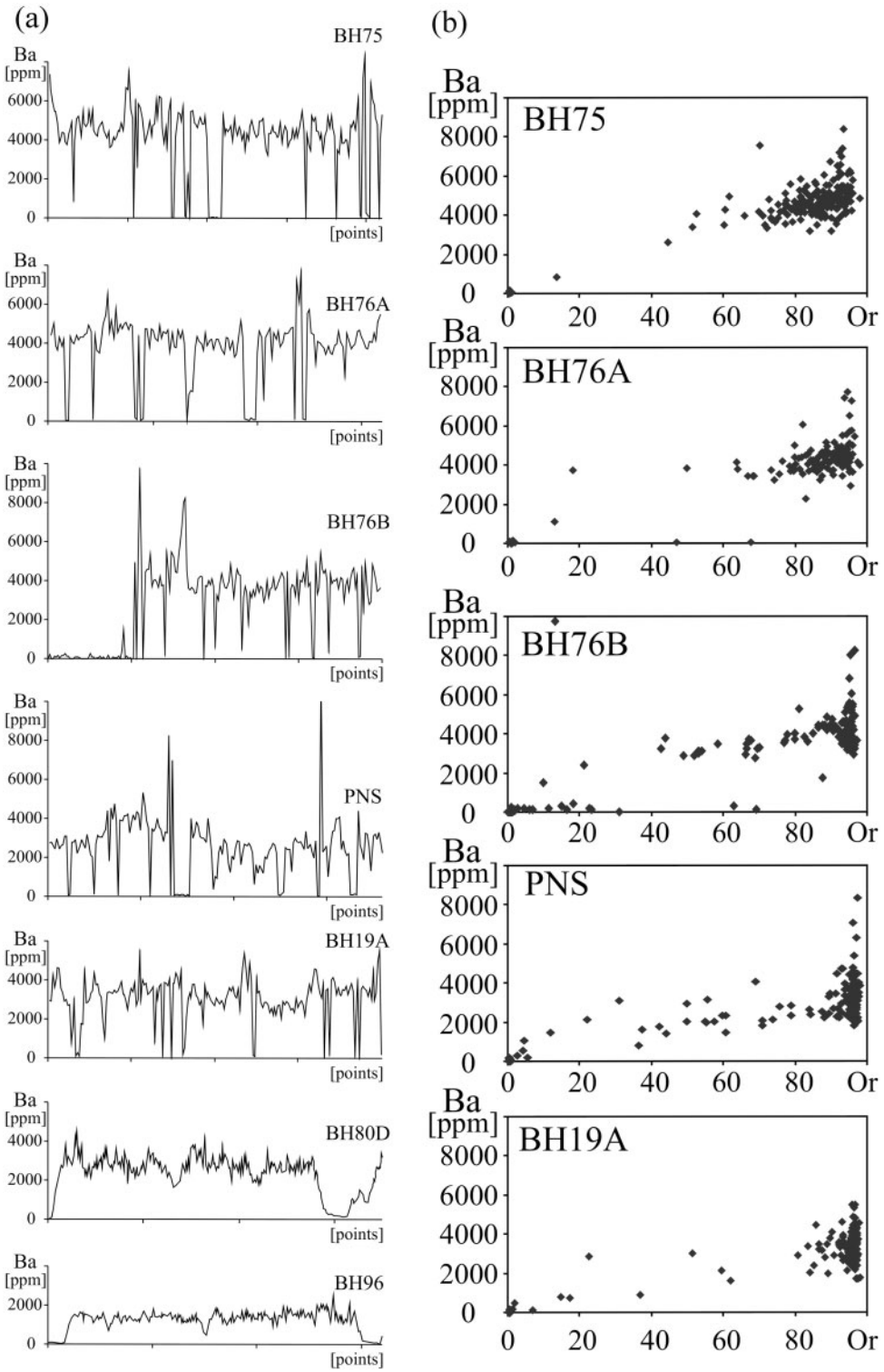

Fig. 8. Megacryst geochemistry: (a) Ba concentration along margin to margin transects; (b) relationship between Ba concentration and orthoclase content shown for selected, representative samples.

Table 3: Oxygen and carbon isotopic composition of alkali feldspars and carbonates

Sample	δ^{18}O‰ VSMOW Transparent domains	δ^{18}O‰ VSMOW Dusty pink domains
Feldspars		
BH75	7·4	7·1
	7·4	7·6
	7·5	7·7
	7·6	7·6
	7·5	7·6
	7·4	7·7
	7·6	
BH171		6·9
		6·9
		6·7
		7·0
		7·2
		7·3
		7·8
		7·6

Sample	δ^{13}C‰ VPDB	δ^{18}O‰ VPDB	δ^{18}O‰ VSMOW
Carbonates			
BH100F	−5·72	−29·53	9·70
BH76A	−4·32	−14·75	15·65
BH75	−4·32	−20·59	9·64
BH76B	−5·44	−17·83	12·48
PNS	−5·20	−20·50	9·73
BH80C	−5·13	−21·75	8·44
BH80D	−4·97	−21·52	8·67
BH96	−5·59	−21·44	8·76
BH171	−5·44	−14·64	5·77

Christoffersen *et al.*, 1983; Cole & Chakraborty, 2001). We observe in the feldspars almost complete Na–K replacement in the dusty pink domains, so it can be assumed that the oxygen isotope exchange was completed earlier. In addition, alkali exchange at high temperatures favours K (Iiyama, 1965, 1968). The turbid domains thus should be almost pure potassium feldspar.

Late structural and geochemical re-equilibration in the alkali feldspars was accompanied by simultaneous carbonate crystallization, suggesting a bimodal H_2O–CO_2 composition for the fluid. As mentioned above, carbon isotopes in carbonates are very homogeneous (δ^{13}C V-PDB $= -5{\cdot}13 \pm 0{\cdot}5$‰); these values are comparable with those of carbonatites, suggesting a mantle origin for the fluids. This conclusion is consistent with measured δ^{18}O values that, although slightly higher than typical mantle values (Taylor *et al.*, 1967; Tichomirowa *et al.*, 2006), point to a high-temperature process. The heavier oxygen isotope values of some carbonates (sample BH76A, BH76B) might be explained by alteration at lower temperatures (Deines, 1989; Santos & Clayton, 1995; Pili *et al.*, 1997*a*, 1997*b*; Tichomirowa *et al.*, 2006).

Fluid composition

IR studies

Reduced defect densities in the marginal parts of feldspar, crystallization of carbonates and chlorine-enriched parts of apatite argue for a binary H_2O–CO_2, halide-rich solution causing the alterations. Of the three components, only water can enter the feldspar structure. For the identification of water or hydrogen species in the magmatic and the re-equilibrated domains, mid-IR spectra (2900–3600 cm^{-1}) were collected on the K-feldspar megacrysts and on one plagioclase megacryst (Figs 9 and 10).

The spectra show striking differences between the turbid and clear regions (Figs 9 and 10); clear regions have single-band (~3300 cm^{-1}) patterns, whereas turbid regions may be converted into a double-band pattern. Initially, the ~3300 cm^{-1} band intensity increases and its shape turns into an asymmetric spectrum (BH75; arrow in Fig. 10). With increasing reaction progress a new band appears at around 3600 cm^{-1} although the band at around 3300 cm^{-1} still dominates. In the strongly dusty pink domains the ~3600 cm^{-1} peak shifts to a higher wavenumber. It also becomes more intense than the ~3300 cm^{-1} peak (BH80C-D, BH96; arrows in Fig. 10). The former (~3300 cm^{-1}) is asymmetric and seems to present a multi-band arrangement (e.g. BH80C), indicating a more complicated water species pattern.

Various structural water speciations can be distinguished and quantified from the characteristics of the broad mid-IR bands (Johnson & Rossman, 2003). Nakano *et al.* (2001) assigned the water species in turbid feldspar areas to non-structural water, generally to fluid inclusions, and to a lesser extent to structural OH groups. The results of our investigation point to a different relationship between the structural and non-structural species. Fluid inclusions in the turbid regions were not observed and no fine-grained alteration products (phyllosilicates) were detected under optical and electron microscopes. However, the rapid increase of the ~3600 cm^{-1} narrow band suggests the presence of both, probably at submicron size (Johnson & Rossman, 2003, 2004).

The growing bands (3200–3600 cm^{-1}) in the turbid areas also point to an increasing variability of the

incorporated structural hydrogen speciation, probably OH groups and molecular water (Fig. 10; Johnson & Rossman, 2003, 2004). CL studies show that structural water may significantly compensate defects in the feldspar structure, lowering luminescence and thus indicating an increase of structural hydrogen speciation during recrystallization (Graham & Elphick, 1990; Kronenberg *et al.*, 1996).

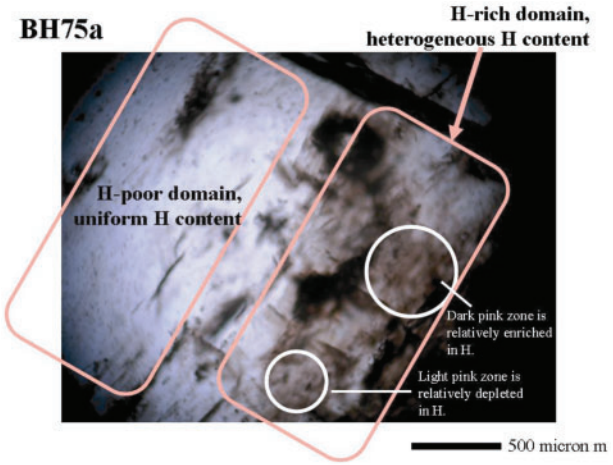

Fig. 9. Section of BH75 megacryst showing domains selected for IR studies.

The appearance of the variety of hydrogen species in the recrystallized domains is critical proof that recrystallization proceeded as a result of fluid–mineral reactions. The spectra show also that the recrystallization process affects both the plagioclase megacryst from the cumulate (BH100F) and alkali feldspar from all the investigated samples, regardless of the degree of differentiation of the host magma. In other words, the efficiency differs between samples, with no relationship to the mechanism of magma differentiation. The cumulate plagioclase's (BH100F) interaction with fluid seems to have been more efficient than in the alkali feldspars, which may point to a continuous post-magmatic process with variable timing or fluid–rock ratios.

Water content—dehydration experiment

Water species are incompatible in feldspar and can be incorporated only in small amounts during magmatic crystallization (Nakano *et al.*, 2001; Johnson & Rossman, 2003). They may enter the feldspar structure during hydrothermal alteration (Yund & Anderson, 1978; Farver & Yund, 1990; Johnson & Rossman, 2003). Consequently, the domains that interacted with fluids should contain higher

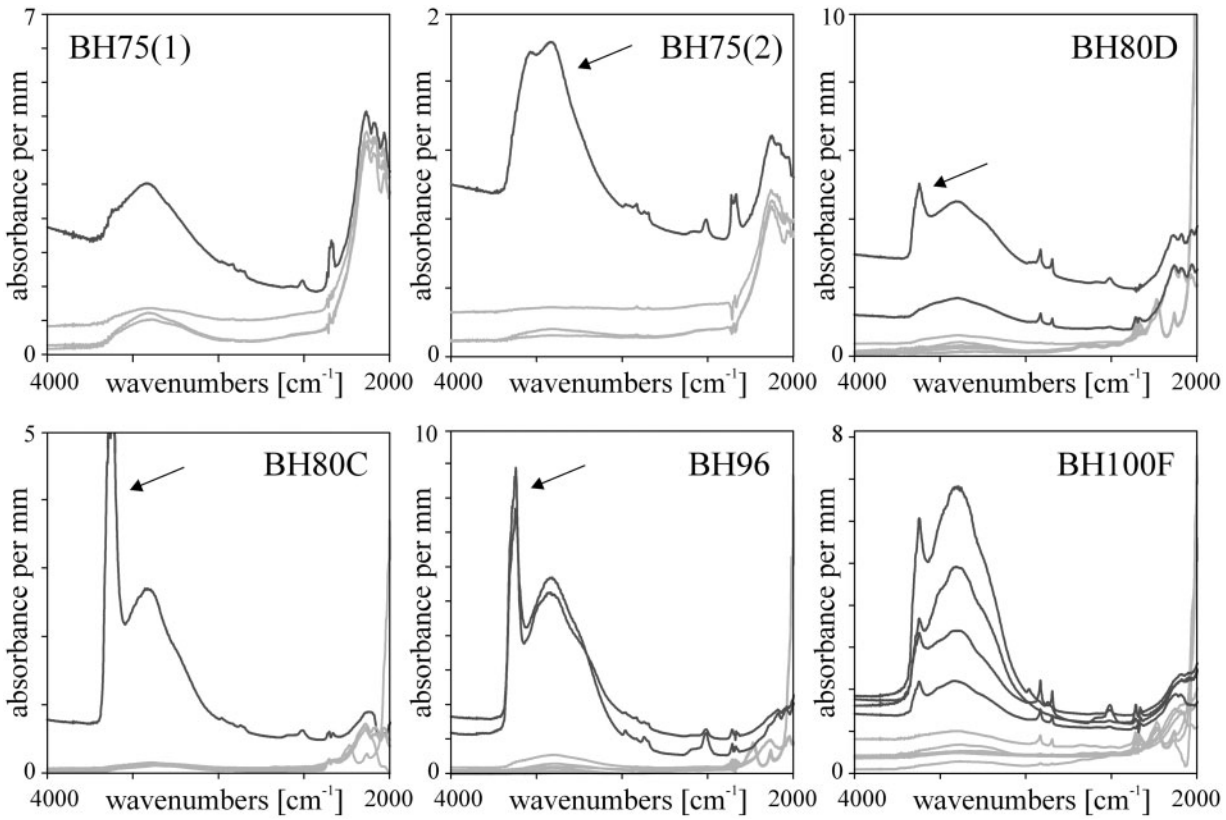

Fig. 10. Selected raw, unpolarized mid-IR spectra collected on clear (light grey spectra) and turbid (dark grey spectra) feldspar domains.

amounts of water compared with pristine magmatic domains. The generally accepted method of quantifying the water content in feldspar is to measure the IR absorption band areas in polarized spectra from three perpendicular directions. In this study, however, we apply a simpler and less precise method to mutually relate the texture of the K-feldspar megacrysts and the IR absorbance. Integrated absorbance values (total areas) were calculated for the fitted spectra above the linear base-line (column 3 in Table 4). The spectra were then deconvolved to separate the constituent peaks at 3200 cm^{-1}, 3400 cm^{-1} and 3600 cm^{-1}. The area of deconvolved peaks was calculated (columns 6–8 in Table 4). In the asymmetric band separated to 3200 cm^{-1} and 3400 cm^{-1} the first dominates. The integrated intensity of the last peak at 3600 cm^{-1} is usually the smallest (Table 4).

According to Johnson & Rossman (2003), a line slope of 0·15 ppm cm^2 can be fitted through data for K-feldspars containing structural water up to 1400 ppm H_2O:

$$\text{water content in feldspar (ppm } H_2O \text{ by weight)} = (0 \cdot 15 \pm 0 \cdot 01) \times A\,(\text{cm}^{-2}) \quad (1)$$

where A is the unpolarized IR band area on (001) per unit thickness (Fig. 11). For the lower hydrogen concentrations in the clear region, we compared both the water concentration determined from the polarized spectra of any three perpendicular directions proposed by Johnson & Rossman (2003) and the unpolarized band area for seven selected feldspars (BH75A, BH75C, BH76B, BH80C, BH171, BH96 and BH100F). The following relationship was found:

$$\text{water content in feldspar (ppm } H_2O \text{ by weight)} = (0 \cdot 23 \pm 0 \cdot 07) \times A\,(\text{cm}^{-2}) \quad (2)$$

where A is the unpolarized IR band area on an optional feldspar plane per unit thickness.

Figure 11 shows that the water concentration of a sanidine feldspar reported by Johnson & Rossmann (2003) and those of the Closepet feldspars fall on a common trend, supporting the notion that the hydrogen concentration in the clear regions of the feldspars can be measured by the unpolarized IR band area on optional feldspar planes, using equation (2). In this study we have used both equations (1) and (2) to estimate the water content in the turbid and the clear areas (Table 4).

The total water content of the clear regions of the feldspar is lower than that of the turbid regions. As shown in Table 4, the water content of the clear regions increases up to ~900 ppm H_2O during magmatic differentiation, whereas in the turbid region it is as high as ~8200 ppm H_2O. The turbid regions with IR band area more than 10 000 cm^{-2} were not converted to water content because that exceeds the calibrated range. The maximum recorded integrated band area for the turbid regions exceeded, however, 24 000 cm^{-2}, indicating a much higher amount.

In situ, high-temperature IR analyses of two selected dusty pink domains in feldspar megacryst (BH76B) were carried out at steps of ~100°C (Fig. 12). During heating, the area of all peaks (~3200 cm^{-1}, ~3400 cm^{-1} and ~3600 cm^{-1}) diminished progressively (Table 5). Band ~3600 cm^{-1} shows the fastest area reduction at relatively low temperature. The process slows down above 400°C. Similarly, the species registered as the asymmetric ~3400 cm^{-1} band leave the feldspar structure comparably quickly and then the rate slows down above 400°C. The reduction of the ~3200 cm^{-1} peak is characterized by slow and stable steps; however, the higher the temperature (700–800°C) the more resistant the behaviour is observed for this water species.

The high-temperature IR analyses performed on two distinct turbid feldspar domains (BH76b-I and BH76b-II) give more precise information on the path whereby water species leave the feldspar structure. This path provides further arguments for the existence of many structural species next to non-structural ones. Whereas the experimental study of Nakano *et al*. (2001) showed that water is almost totally removed from turbid domains below 300°C, our results indicate that in some domains (Table 5; BH76B–I), 60–70% of the water remains above 300°C. The path of water release during heating at higher temperatures and the high integrated absorbance of the 3600 cm^{-1} band in the spectra collected between 600 and 800°C argue in favor of a considerable contribution by structural water in the re-equilibrated feldspar domains. This leads to the conclusion that the band position around 3600 cm^{-1} can be related to structural H_2O and not to a non-structural species (Johnson & Rossman, 2004). The high-temperature spectra show the presence of water even at temperatures as high as 800°C, which is close to magmatic crystallization conditions. Changes of the spectra are reversible, at least up to temperatures of 600°C; this finding suggests that fluid–granite interactions took place at about 600°C or even higher, consistent with the conclusion drawn from oxygen isotopes.

Trace element composition of fluids—3D depiction of the LA-ICP-MS data

Selected crystals were analyzed along several transects from margin to margin, giving simultaneous information on the concentration of many elements from the same analysed crystal volume. The data from areas enriched in barium have been used to reconstruct the trace element composition of the fluid. Selected data for clear and turbid domains of feldspars are given in Table 6.

Maps of the spatial distribution of Ba, Sr and Rb (Fig. 13) were built up from a base of six parallel transects (~1600 points each). In contrast to the EMPA single

Table 4: Element concentrations (ppm) in water-clear and turbid feldspar domains; LA-ICP-MS selected data

^{31}P	^{49}Ti	^{55}Mn	^{57}Fe	^{85}Rb	^{88}Sr	^{89}Y	^{90}Zr	^{133}Cs	^{137}Ba	^{139}La	^{140}Ce	^{151}Eu	^{208}Pb	^{232}Th	^{238}U
Sample BH80D, turbid															
39·9	9·1	2·3	169·1	242·7	271·5	0·0	0·3	2·0	3588·5	0·9	0·2	0·3	48·6	0·0	0·5
55·0	26·3	3·2	265·9	310·8	317·9	0·1	0·0	2·2	3591·6	0·7	0·4	0·2	36·1	0·1	0·1
44·6	28·8	0·7	140·2	227·2	318·5	0·0	0·0	0·7	3601·9	0·3	0·0	0·5	33·1	0·2	0·1
31·5	10·0	0·7	137·1	248·6	229·7	0·1	0·1	1·3	3612·8	0·5	0·3	0·7	34·8	0·0	0·2
66·4	33·8	0·5	145·8	161·5	271·1	0·1	0·0	0·8	3613·2	0·6	0·3	0·3	19·8	0·0	0·0
43·9	49·1	2·4	374·8	217·6	216·0	0·0	0·1	1·6	3650·2	0·3	0·1	0·2	26·1	0·3	0·1
21·3	15·6	4·9	529·5	211·0	512·0	0·0	0·2	1·4	3667·5	0·4	0·2	0·3	37·0	0·2	0·2
48·0	25·9	0·6	97·4	221·0	226·9	0·2	0·1	1·3	3681·6	1·0	0·1	0·4	32·2	0·2	0·0
26·2	17·8	0·3	95·4	178·6	214·3	0·1	0·2	1·4	3690·5	0·5	0·1	0·1	45·5	0·0	0·0
20·0	11·3	0·9	154·2	204·6	270·6	0·0	0·1	1·2	3698·8	0·5	0·1	0·2	26·1	0·0	0·1
27·9	27·1	6·5	354·0	192·6	187·1	0·3	0·0	1·3	3699·1	2·6	2·3	0·6	43·3	0·1	0·3
36·7	17·0	1·5	127·9	243·0	307·8	0·1	0·2	1·4	3835·9	0·4	0·0	0·3	26·4	0·3	0·8
43·2	21·6	0·3	150·7	237·2	351·9	0·0	0·1	0·7	3836·0	0·4	0·0	0·2	36·1	0·0	0·2
79·6	24·6	0·6	132·8	164·2	236·5	0·6	0·0	1·1	3843·6	3·4	1·7	0·3	23·0	0·5	0·2
15·5	28·4	0·6	174·1	223·3	291·6	0·3	0·1	0·7	3847·9	0·5	0·2	1·2	28·4	0·1	0·1
66·3	51·9	1·1	108·8	204·3	235·5	0·4	0·2	1·5	3862·8	2·7	0·8	0·7	35·7	0·3	0·3
51·9	27·0	0·8	273·7	168·6	206·0	0·1	0·0	0·7	3907·7	0·5	0·0	0·1	29·6	0·0	0·0
54·9	24·7	0·4	148·4	231·7	378·0	0·0	0·0	1·1	4271·4	0·6	0·1	0·0	38·2	0·0	0·2
43·3	21·4	0·5	191·1	209·1	337·5	0·1	0·0	0·7	4306·3	0·6	0·3	0·7	35·0	0·2	0·1
30·5	24·5	0·6	190·5	228·0	317·4	0·1	0·1	1·4	4538·8	0·4	0·1	1·0	31·7	0·1	0·0
Sample BH19A, turbid															
11·6	26·3	1·8	373·2	268·1	406·0	0·2	0·0	1·7	2925·9	3·6	1·3	0·4	47·4	0·1	0·2
8·9	11·0	24·0	96·0	379·6	434·3	0·1	0·0	0·8	2926·4	0·9	0·5	0·1	55·6	0·1	0·2
15·0	24·6	53·9	81·0	332·6	552·2	0·1	0·0	0·9	2937·8	1·3	1·1	0·4	58·7	0·1	0·0
46·4	15·6	5·3	66·9	220·0	309·8	0·2	0·3	0·3	2941·2	0·6	0·4	0·0	38·7	0·1	0·4
24·6	30·5	4·8	85·7	278·2	317·2	0·2	0·0	0·6	2948·8	0·3	0·1	0·2	41·9	0·0	0·4
35·3	11·7	13·8	71·8	226·2	285·5	0·1	0·1	0·4	2955·7	0·6	0·3	0·1	42·9	0·0	0·0
17·6	18·3	65·6	53·8	196·8	342·6	0·2	0·1	0·7	2957·5	0·6	0·6	0·1	42·7	0·1	0·0
27·9	13·7	5·0	90·7	190·0	293·7	0·1	0·1	0·5	2962·7	0·2	0·2	0·0	29·6	0·0	0·3
42·0	12·1	25·9	87·0	183·7	255·7	0·1	0·1	0·8	3007·8	0·3	0·6	0·1	42·4	0·0	0·1
27·1	12·2	5·8	61·1	247·3	310·0	0·1	0·0	0·8	3038·4	0·5	0·1	0·0	35·0	0·0	0·1
45·5	16·8	3·5	48·7	398·5	298·0	0·1	0·0	0·7	3038·8	0·4	0·1	0·0	42·6	0·3	0·0
59·7	12·6	24·5	56·5	265·2	354·6	0·3	0·0	0·9	3080·7	0·6	0·9	0·1	41·0	0·0	0·2
21·9	8·2	2·4	55·6	171·5	239·8	0·1	0·1	0·4	3081·2	0·5	0·1	0·0	26·9	0·1	0·0
Sample BH75C, turbid															
33·6	11·0	8·2	59·2	183·9	372·7	0·2	0·0	0·9	3110·0	0·6	0·3	0·1	49·8	0·1	0·2
36·3	15·8	12·9	53·0	207·8	304·8	0·1	0·0	0·5	3112·0	0·4	0·8	0·1	47·2	0·2	0·2
23·9	25·2	11·6	75·6	264·2	220·4	0·1	0·0	0·6	3116·3	0·2	0·0	0·0	37·2	0·1	0·1
11·9	12·2	3·5	34·7	193·2	230·5	0·1	0·1	0·7	3123·7	0·5	0·0	0·1	24·8	0·0	0·0
24·9	24·1	8·2	58·3	222·8	343·2	0·2	0·3	0·7	3164·0	0·8	1·4	0·0	30·1	0·1	0·1
6·9	18·3	7·7	53·7	198·1	271·0	0·1	0·0	0·7	3212·3	0·6	0·2	0·3	32·3	0·0	0·0
26·7	21·1	4·7	62·4	293·5	337·6	0·1	0·0	0·6	3306·5	0·4	0·3	0·1	37·4	0·2	0·3
31·2	19·8	74·7	37·2	240·8	380·0	0·1	0·0	0·8	3310·3	0·8	0·5	0·1	47·5	0·1	0·0
63·4	13·4	9·4	45·4	235·9	389·1	0·1	0·1	1·6	3387·9	0·5	0·8	0·1	55·1	0·1	0·0
32·4	18·2	102·0	105·2	219·4	377·9	0·1	0·1	0·8	3462·9	1·1	0·5	0·1	57·3	0·0	0·2
36·1	17·9	34·4	81·8	351·6	571·0	0·2	0·0	0·9	3603·1	0·9	0·3	0·1	55·1	0·2	0·0

(continued)

Table 4: Continued

^{31}P	^{49}Ti	^{55}Mn	^{57}Fe	^{85}Rb	^{88}Sr	^{89}Y	^{90}Zr	^{133}Cs	^{137}Ba	^{139}La	^{140}Ce	^{151}Eu	^{208}Pb	^{232}Th	^{238}U
Sample BH80D, clear															
33·9	13·7	-0·1	130·2	219·8	167·0	0·0	0·1	2·3	1883·4	0·2	0·1	0·1	32·4	0·1	0·4
38·5	17·9	0·8	165·5	188·4	223·8	0·0	0·6	1·8	1887·0	0·3	0·2	0·1	28·1	0·0	0·1
27·9	6·8	3·3	108·4	163·4	130·6	0·0	0·0	1·1	1891·4	0·3	0·0	0·1	18·7	0·1	0·0
22·2	67·3	80·3	110·3	164·8	190·8	0·0	0·1	1·1	1891·8	0·2	0·2	0·1	22·7	0·0	0·1
43·9	13·3	2·3	133·5	192·9	202·2	0·1	0·1	1·9	1892·1	1·0	0·4	0·1	25·4	0·0	0·2
22·6	24·2	0·7	152·0	150·9	307·6	0·0	0·0	0·7	1892·6	0·2	0·1	0·4	24·1	0·0	0·1
36·1	32·6	0·2	154·1	219·6	204·0	0·1	0·9	0·9	1893·0	0·3	0·1	0·2	25·4	0·1	0·2
45·3	25·7	1·9	193·4	202·7	195·0	0·0	0·2	1·6	1895·9	0·4	0·0	0·2	24·6	0·0	0·1
19·6	27·1	9·9	215·0	188·6	228·7	0·0	0·1	0·9	1896·7	0·3	0·0	0·1	25·8	0·0	0·1
24·8	28·0	2·6	352·3	166·8	322·1	0·0	0·1	1·1	1897·4	1·0	0·6	0·1	22·4	0·1	0·0
39·3	17·1	0·1	81·9	131·1	195·1	0·0	0·0	0·8	1900·7	0·2	0·0	0·2	13·5	0·0	0·2
36·2	25·0	6·1	81·5	219·7	240·0	0·0	0·0	0·4	1901·2	0·2	0·0	0·1	23·3	0·1	0·0
Sample BH19A, clear															
50·1	14·1	0·6	133·6	202·3	335·7	0·0	0·0	0·8	1911·9	0·3	0·2	0·1	22·4	0·1	0·1
92·8	3·6	2·5	227·1	205·0	174·4	0·0	0·2	0·8	1915·7	0·5	0·6	0·1	14·8	0·0	0·2
30·2	26·5	0·9	423·1	242·5	289·9	0·0	2·0	1·1	1916·8	0·5	0·2	0·1	27·0	0·0	0·2
20·3	14·4	0·6	202·4	181·5	209·7	0·0	0·0	1·2	1918·1	0·4	0·1	0·1	25·7	0·0	0·1
26·4	17·4	3·7	100·6	184·4	212·2	0·0	0·0	1·2	1920·8	0·2	0·0	0·2	24·4	0·0	0·0
47·8	24·2	1·3	220·6	175·9	345·3	0·1	0·0	0·7	1922·4	0·2	0·2	0·4	20·1	0·0	0·1
14·7	14·5	2·1	73·0	222·5	200·0	0·0	0·0	0·8	1923·0	0·2	0·1	0·1	26·3	0·0	0·0
Sample BH75C, clear															
30·3	7·7	2·3	185·4	131·7	360·8	0·0	0·1	0·8	1930·5	0·5	0·3	0·1	15·4	0·3	0·0
52·4	24·6	0·5	210·6	238·6	250·3	0·0	1·4	2·0	1931·1	0·2	0·0	0·2	28·1	0·1	0·3
37·4	3·4	0·4	69·5	108·7	165·5	0·0	0·0	0·3	1932·0	0·0	0·1	0·0	8·0	0·0	0·1
32·7	17·5	0·3	161·7	156·1	233·3	0·0	0·7	1·4	1933·4	0·5	0·2	0·0	23·3	0·1	0·1
38·0	17·3	3·4	244·6	197·4	258·1	0·0	9·6	2·1	1935·9	0·5	0·4	0·2	22·8	0·0	0·3
25·4	15·0	81·2	132·3	133·6	163·1	0·0	0·0	0·4	1937·3	0·2	0·2	0·0	19·8	0·0	0·1
21·4	10·1	1·0	119·8	165·1	256·7	0·1	0·6	1·4	1938·1	0·2	0·4	0·2	14·8	0·1	0·4
60·4	24·1	0·3	165·2	176·0	255·5	0·0	4·6	1·4	1940·3	0·7	0·2	0·1	22·7	0·1	0·0

profiles across each crystal, which seem to indicate crystallization from chemically blended magmas, the mapped surfaces show extensive roughness. First, from a technical point of view, this result indicates that a single EMPA traverse cannot be considered as sufficiently representative for element distribution in megacrysts; more profiles are required to map reasonably well the element distribution.

Figure 13a–d reveals the heterogeneous distribution of trace elements in a single K-feldspar crystal. The pattern is similar for Ba and Sr but different for Rb (Fig. 13a and b). The margin of the crystal (left side of the image) shows irregularly distributed high Ba and Sr contents, whereas these patterns are very much attenuated or even absent in the core (right side) of the crystal. In fact, the Sr and Ba distributions are not totally irregular and the peaks of high content in these elements are distributed along parallel, precisely located, and common paths (arrows in Fig. 13a and b). Barium enrichment surpasses that of Sr. In contrast, the pattern of Rb distribution takes the form of irregular patches; however, the Rb map shows that Rb content is slightly greater on the rims than in the core of the megacrysts.

Homogeneous magmatic growth textures seem to be obscured by fluid-induced reactions, which supplied some of the elements to selected regions, causing an exchange and an enrichment along preferred crystallographic orientations and cracks. Regions enriched in Ba and Sr are also enriched in LREE, Pb and Y (the statistics are based on 1500 point measurements in each profile crossing both pristine and fluid-recrystallized crystal parts).

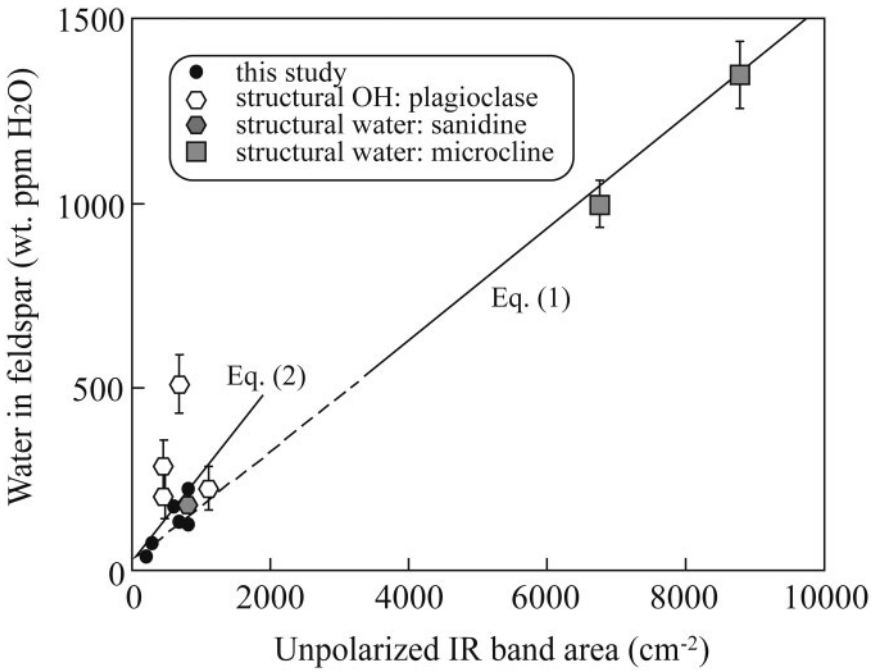

Fig. 11. Unpolarized IR band area vs water concentration in feldspar. Sanidine–microcline data taken from Johnson & Rossman (2003).

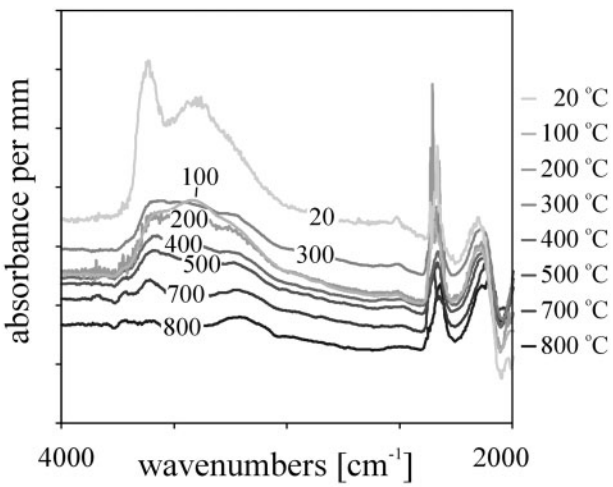

Fig. 12. High-temperature IR analyses. Spectra are shifted vertically for comparison.

The enrichment of P, U, Th and Zr is, however, less consistent; some turbid domains are enriched, whereas others are similar to magmatic concentrations. It is noteworthy that magmatic–translucent domains contain many inclusions of accessory minerals, which are P–U–Th–Zr bearing.

As noted for the EMPA profiles, high trace element concentrations cannot result from fractional crystallization or mixing but seem to be controlled by fluids that invaded the megacrysts from rim to core, using cracks and cleavages as favoured paths The existence of channels implies that the enrichment event took place after feldspar crystallization. The spatial pattern of trace element distribution seems to reflect the textures recognized in CL images. Digital trace element concentration distribution models can thus be more efficient in recognizing recrystallization textures than other imaging techniques, especially if recrystallization does not drastically change the major element composition.

Growth and regrowth textures reconstructed by digital trace element distribution models

The 3D depiction of trace element distribution (Fig. 13) allows us to decipher in detail the mechanism of crystal growth and regrowth. Indeed, if some features of the feldspar megacrysts can easily be attributed to crystallization from a magma, others point to an enrichment event that took place after feldspar crystallization. A crucial point consists of determining whether the observed late textures were related to late-stage magma differentiation or if they result from recrystallization induced by an unrelated fluid.

To discriminate between the above processes, we analysed the textures assumed to be linked to the latter process. This analysis is based on maps of the maximum gradient value (Fig. 13c) and of the direction of the maximum gradient (Fig. 13d). Both illustrate the dynamics of the variation in element concentrations. They also allow the precise identification of places where the most intensive

Table 5: Summary of the IR investigations

Sample		Absorbance (cm^{-2})	Equation	Hydrogen (ppm H_2O by weight)	Integrated absorbance of deconvoluted spectra (cm^{-2})		
					3200 cm^{-1}	3400 cm^{-1}	3600 cm^{-1}
1	2	3	4	5	6	7	8
BH75	clear	400	(2)	92 ± 28	235	114	32
	turbid	1603	(1)	241 ± 16	1085	861	58
	turbid	4121	(1)	618 ± 41	1990	1740	999
	clear	316	(2)	73 ± 22	227	79	27
BH76B	turbid	1054	(1)	158 ± 11	697	299	126
	turbid	4533	(1)	680 ± 45	1743	904	1506
	clear	570	(2)	131 ± 40	341	181	38
BH80C	turbid	23138					
	clear	690	(2)	159 ± 48	305	166	50
	clear	440	(2)	101 ± 31	305	166	50
	turbid	3927	(1)	589 ± 39	2181	912	982
	turbid	525	(1)	79 ± 5	337	125	53
	turbid	1186	(1)	178 ± 12	979	226	233
BH96	clear	980	(2)	225 ± 69	675	126	197
	turbid	16949					
	turbid	18338					
BH100F	clear	563	(2)	129 ± 39	522	384	148
	clear	1056	(2)	243 ± 74	276	234	70
	turbid	648	(1)	97 ± 6	3764	1814	1438
	turbid	8219	(1)	1233 ± 82	12268	5177	3780
	turbid	24777					
	turbid	4049	(1)	607 ± 40	8500	3792	1968
BH171	clear	400	(2)	92 ± 28			
	turbid	1765	(1)	265 ± 18	936	857	105
	turbid	6581	(1)	987 ± 66	3827	2362	1333

Estimated water contents of feldspar using equations (1) and (2) are shown in column 5. Turbid regions with absorbance of >10 000 cm^{-2} were not converted to water content because they exceed calibration range of equation (1). Integrated absorbance obtained after spectra deconvolution (peaks 3200 cm^{-1}, 3400 cm^{-1}, 3600 cm^{-1}) are shown in columns 6–8.

chemical change took place in the feldspar megacrysts. Both the value and the direction of the maximum gradient for a grid node are properties of a tangent plane to a point on an interpolated surface, which quantifies the element concentration variability. In other words, the direction of the maximum gradient is an azimuth of a maximum gradient line (e.g. local greatest rate of change in element concentration; Fig. 13d), and the maximum gradient value is the dip angle of that line (Fig. 13c).

The localization of variations in Ba and Sr contents appears clearly in Fig. 13c and d, being better defined with the simultaneous use of both depiction techniques. Gradients of the change in Ba and Sr display a regular arrangement on the left side of the maps (crystal margin), where continuous and straight sectors, outlined with rectangles, of very low gradient, are bordered by zones of higher gradient (Fig. 13c). Their continuous right–left extent breaks up toward the crystal core into a discontinuous pattern of local, ring-shaped minima and maxima. The ring-like shape is a consequence of the appearance of local 'hills' with steep slopes on each side. The left–right extended sectors clearly indicate intensive and efficient reaction with the external agent strongly enriched in Ba and less rich in Sr (the slope of the gradient vector changes from 55° up to 85°). These local changes completely obliterated the original geochemical signatures and relationships. In contrast to Ba and Sr, Rb does not show a regular distribution: the maximum gradient is low with a slope less than 15°.

Consequently, it appears that for Ba and Sr the pattern of high exchange efficiency is superimposed on a pristine pattern characterized by low efficiency. Rb distribution

Table 6: Heating experiment performed on two turbid domains in the megacryst BH76B

Sample	T (°C)	A (cm^{-2})	Integrated absorbance (cm^{-2})		
			3200 cm^{-1}	3400 cm^{-1}	3600 cm^{-1}
1	2	3	4	5	6
BH76B-I	20	4729	–	–	–
	100	3533	160	101	43
	200	2991	129	102	32
	300	2564	118	72	26
	400	2194	83	63	28
	500	1766	58	50	22
	600	1339	43	29	16
	700	1026	33	17	11
	800	655	–	–	–
BH76B-II	20	3390	278	208	41
	300	1311	116	56	20
	400	1339	133	50	23
	500	855	72	45	20
	600	712	43	37	13
	700	almost 0	–	–	–

Integrated absorbance obtained after spectra deconvolution (peaks 3200 cm^{-1}, 3400 cm^{-1}, 3600 cm^{-1}) are shown in columns 4–6.

does not show significant changes, meaning that the pristine pattern is better preserved. Similarly, in the left-hand part of the map illustrating the directions of the maximum gradient for Ba and Sr (Fig. 13d), some sectors can be identified transverse to the lateral line of the LA-ICP-MS transect. The opposite gradient directions are labelled with bright and dark colours. The regular patterns related to the marginal part of the crystal progressively disappear towards the core. Here, too, Rb shows weaker organization, with no clear trend of the gradient change.

Analysis of both the maps of the maximum gradients and of the direction of the maximum gradient supports the hypothesis that the observed anomalies in the element distribution cannot be purely related to magmatic processes or subsolidus re-equilibration with a differentiated volatile-rich magma, but can better be related to two different processes that have little geochemical affinity.

Element behaviour during magmatic crystallization and post-magmatic fluid interaction—fractal statistics

From the whole-rock geochemistry of the Closepet granite, Moyen *et al.* (2001*a*) concluded that its main geochemical features resulted from magma mixing. Magma mixing is a non-linear dynamic system (Perugini *et al.*, 2003, 2005), whose chaotic nature can be evidenced through calculation of the fractal dimension. Fractals refer to self-similarity. The system is self-similar if an arbitrarily chosen part of the system demonstrates similarity to itself. This also means that the parts of the system show statistical self-similarity. Here we use fractal statistics to establish whether the spatial distribution of elements in the feldspar domains (marginal and core) results from self-similar complex phenomena or whether the self-organizing complex system was different during crystallization and during recrystallization. Indeed, the behaviour of trace elements during two contrasted processes, such as magmatic crystallization and post-magmatic recrystallization, will be controlled by contrasted chemical laws.

Maps of Hurst exponent (H) variability for Ba, Sr and Rb (Fig. 14c–h) have been constructed using data pre-selection methods (2) and (3); for example, excluding all inclusions from the megacryst (see the section 'Data processing' and Fig. 14a). The value was calculated separately for sections fulfilling both of the pre-selection criteria and attributed to the central point of each section. Another mode combined the profiles and divided them into three sectors, each containing one zone of element enrichment. The Hurst exponent was attributed respectively to the central point of each sector. The differences in both modes are shown in Fig. 14. Figure 14c, e and g shows maps using the second mode and Fig. 14d, f and h shows maps of the first mode. The lowest H values were calculated for Rb, which varies within a small range (Fig. 14e and f). In contrast, for Ba and Sr, H varies over a wider range, from high H in the margin to low H in the core (Fig. 14c, d, g and h).

The Hurst exponent maps are related to the 3D depiction of element distribution. The left sides of the 3D depiction of element distribution demonstrate greater heterogeneity in element spreading, whereas the right sides are more homogeneous (Fig. 13a and b). The 3D depictions suggest overlapping processes. In all Hurst exponent maps two processes can also easily be recognized. In the core of the megacrysts (right side of the maps; Fig. 14c and d, g and h) the Ba–Sr distribution can be ascribed to magmatic growth (compare with Fig. 13a and b). In contrast, the marginal zones (left side of the maps; Fig. 14c, d, g and h) display a lower degree of chaos, which we can relate to inferred late crystal–fluid interactions (compare with Fig. 13a and b). Both processes are deterministic, not random. The spatial distribution of Ba and Sr in the crystal margins is irregular (Fig. 13a and b). On Hurst exponent maps high H values ($0{\cdot}8 < H < 1{\cdot}0$) identify the process as persistent (Fig. 14c, d, g and h). The trace element distributions in feldspar cores are almost homogeneous and only relatively small and

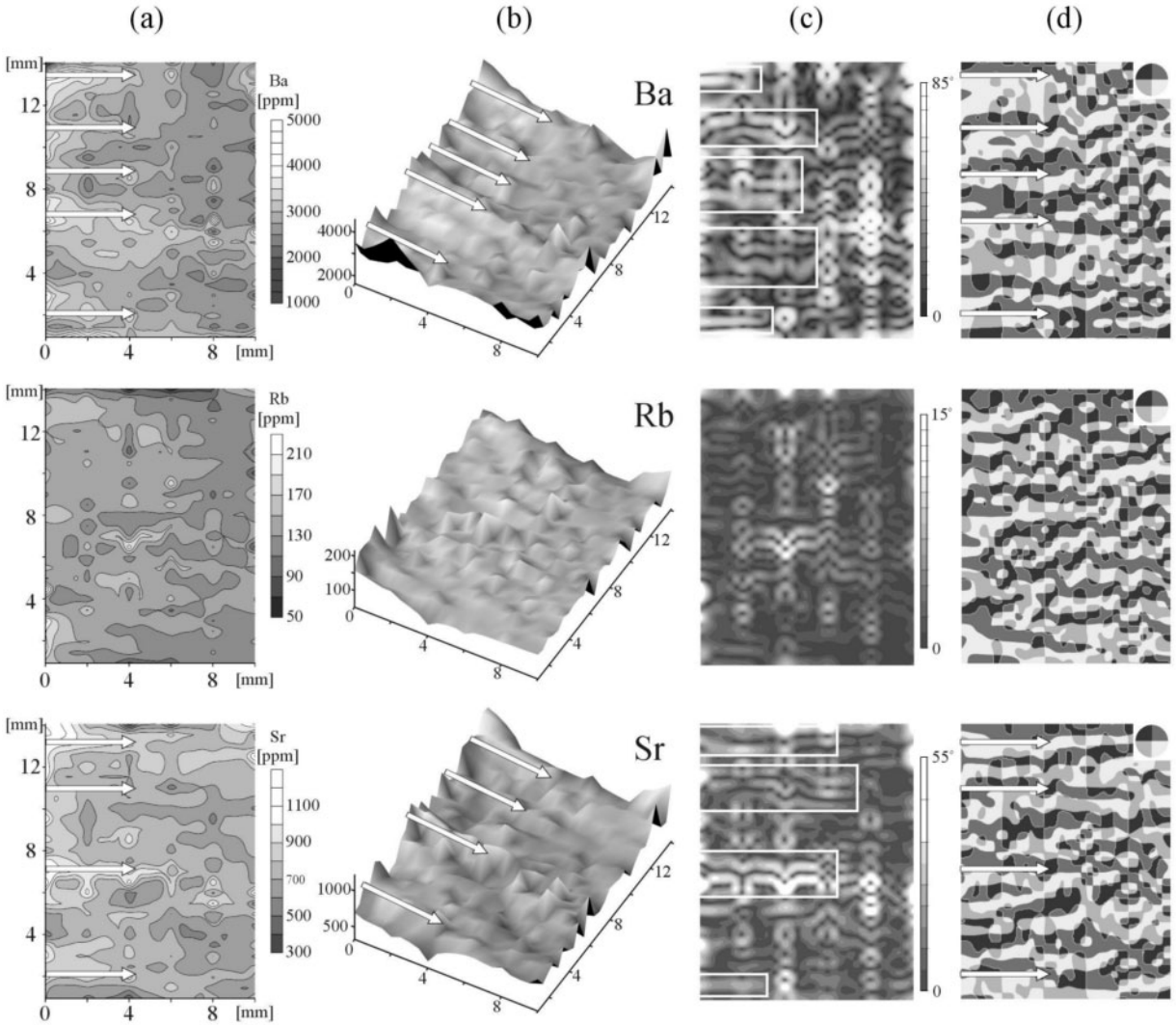

Fig. 13. Spatial depiction of trace element distribution in a K-feldspar megacryst from sample BH76B (from the crystal margin, left side; to the core, right side) based on LA-ICP-MS data. The LA-ICP-MS transects were located parallel to the *y*-axis, the investigated surface was 10 mm × 14 mm. (a, b) Distribution of Ba, Rb and Sr shows that the primary homogeneous growth pattern is obscured by another one: the elements (preferentially Ba and Sr) are exchanged along some linear direction (arrows). (c) Maps of maximum gradient value (expressed as an angular value of a locally greatest rate of an element concentration decrease) identify this process as more dynamic than pristine magmatic crystallization (see Discussion for further explanation). (d) Maps of the direction of maximum gradient (expressed as an azimuth of a line of the locally greatest rate of an element concentration decrease) demonstrate semi-regular, linear sector arrangement on the left side of the map (Ba–Sr), which disappears on the right side; the more patchy right side as well as the Rb map point to undirected, chaotic distribution of the maximum gradient direction values.

irregular variations in trace element contents make their growth morphology slightly patchy (Fig. 13a and b). Despite homogenization, the fractal statistics reveal that trace elements were incorporated chaotically into the growing crystal. The spatial distribution of Rb is almost homogeneous in the crystal core and margin (Fig. 13a and b), testifying to an insignificant change after cessation magmatic crystallization. The Hurst exponent value in turn is low and points to anti-persistent behaviour (Fig. 14e and f).

The differences in Ba, Sr and Rb behaviour cannot be explained by variable element mobility during mixing. Indeed, Perugini *et al.* (2008) and Słaby *et al.* (2011) showed that Rb is the most mobile during mixing events. Rubidium thus tends to homogenize in the mixed magmas before Ba and Sr. The fractal statistics show its anti-persistent behaviour and indicate that feldspar crystallization was a chaotic, self-organizing complex process. If the observed growth textures resulted only from mixing, one might expect Hurst exponent values for

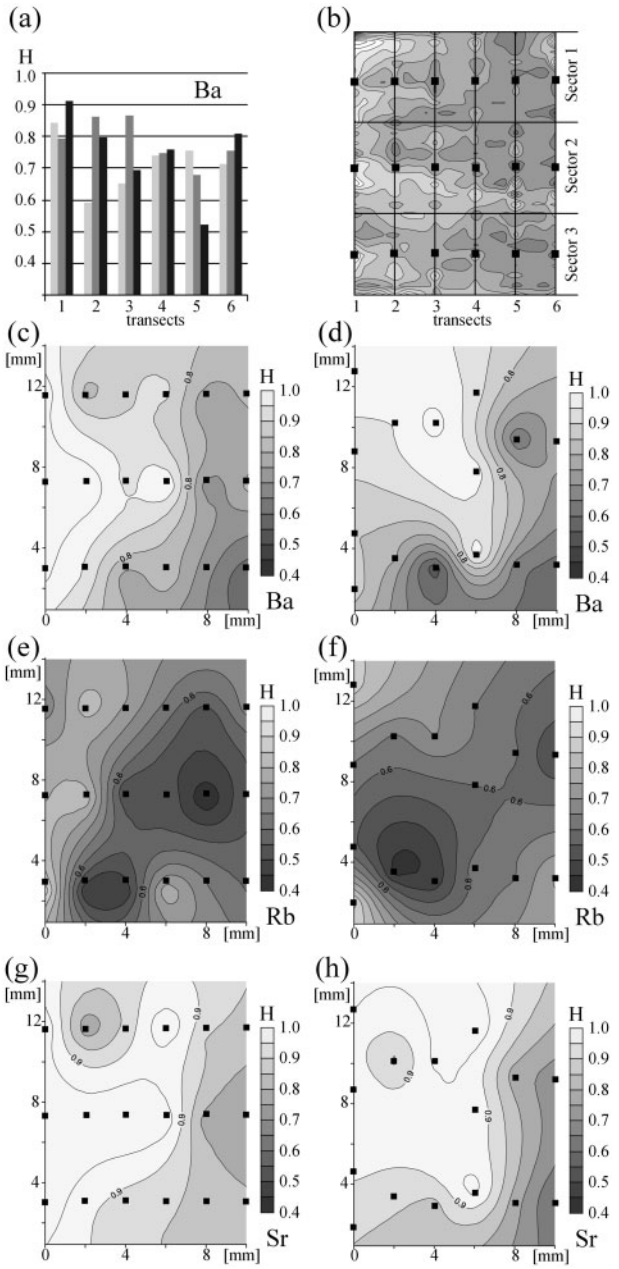

Fig. 14. Self-organized complexity of element distribution during magmatic crystallization and inferred late interaction with fluids. (a) Bar graph illustrating differences in the *H* values calculated according to three methods of data pre-selection; (b) 3D depiction of Ba distribution with superimposed scheme of grid, points and sectors determined for final *H* values estimation (second modes) used subsequently for map arrangement; (c–h) roughness exponent maps of Ba–Rb–Sr spatial distribution: the left row shows the results obtained using the second mode of profile arrangement, the right one shows those obtained using the first mode (note change of position of the central points within sectors); Ba and Sr demonstrate less persistent behaviour during magmatic crystallization and more persistent behaviour during later interaction with fluids, whereas Rb gives evidence for anti-persistent, changing to persistent character; all the trace elements show that the processes were chaotic, not random.

Ba and Sr to be lower than those for Rb: the opposite is observed. For this reason the decoupling of the correlation at a short length scale between Rb and Ba–Sr cannot be explained by simple mixing and points to the operation of another process (Perugini & Poli, 2004; Perugini *et al.*, 2008; Słaby *et al.*, 2011).

The anti-persistent chaotic behaviour of elements during magmatic growth of the feldspars progressively changes into persistent behaviour within domains, where recrystallization reaction took place. Ba and Sr demonstrate the variable dynamics of this exchange corresponding to increasing persistency (Fig. 14c, d, g and h). It is noticeable that Sr, which diffuses more easily (Nakamura & Kushiro, 1998), shows almost perfect persistent character during post-magmatic exchange, whereas Ba does not. Consequently, it appears that fractal statistics clearly discriminate between two processes, with contrasted element behaviour during these processes. One process is magma crystallization and is recorded in the core of the megacrysts; the other is recorded in the crystal rims and along cleavages and cracks; this can be related to a post-crystallization process linked to fluid percolation.

CONCLUSIONS

Granites are formed by a multi-stage process, each stage influencing the equilibrium of the system. The rock chemistry reflects all successive events and therefore methods are required to separate overlapping effects to identify each process involved.

The data presented in this study provide evidence for magmatic crystallization and post-magmatic recrystallization leading to the development of new domains in feldspar crystals. The composition of these new domains cannot be accounted for by a simple magmatic differentiation process. The multi-method approach employed (major element, trace element and isotope geochemistry, IR, CL and 3D depiction of geochemical data and fractal statistics) allows the recognition and the separation of the processes. We paid particular attention to two tools: 3D depiction of geochemical data and fractal statistics. If a process, featuring non-linear dynamics, is overlapped by another process, fractal statistics seems to be the ideal tool to separate these processes. In addition, digital trace element concentration distribution models provide a good approach for the identification of any subsequent change occurring in the system owing to chaotic or non-chaotic processes.

The multi-method approach allows consistency control of the various datasets. A good example would be to take into account IR, EMPA and LA-ICP-MS data, when compared with CL observations. The mechanism to incorporate Ba in feldspar needs to be consistent with fluid activity. Usually barium incorporation is related to the coupled substitution $K^{+} + Si^{4+} \rightarrow Ba^{2+} + Al^{3+}$, which

results in structural distortion and consequently in an increase of defect density, as proposed by Słaby *et al.* (2008). In contrast, the studied recrystallization, proceeding in a high-temperature fluid film through dissolution–reprecipitation (Putnis *et al.*, 2005, 2007; Parsons & Lee, 2009; Parsons *et al.*, 2009; Plümper & Putnis, 2009), results in increasing order and decreasing defect density. The process involves charge compensation by water incorporated in the structural position of oxygen, following the reaction $2K^{+}+O^{2-} \rightarrow Ba^{2+}+2OH^{-}$. The presence of hydrogen enhances Al–Si inter-diffusion, leading to order–disorder and the defect density modification, healing some of them and inducing at the same time a secondary population (Graham & Elphick, 1990; Kronenberg *et al.*, 1996). Both species (OH^{-}–H^{+}) can be incorporated into feldspar during fluid–rock re-equilibration (Johnson & Rossman, 2003) under high-temperature conditions, and can account for the observed CL characteristics, the chemical variations between domains and the oxygen isotope data. Thus, evidence obtained by one method will not give sufficient information about mutual element relationships and even can lead to false conclusions.

Apart from the methodological aspects, this study presents new data on Archaean granites. As mentioned above, the composition of the investigated new feldspar domains cannot be accounted for simply by magmatic differentiation, fractional crystallization or mixing. These domains are K-rich, with a low density of structural defects (e.g. new Si–Al order–disorder pattern). They show new trace element compositions including incompatible water species. In particular, the parts affected by modification are water-rich and enriched in LREE, Y, Pb, Ba and Sr. These trace element signatures preclude late magmatic interaction with internal fluids released after magmatic differentiation, because such fluids would be depleted in these elements, especially in Ba and Sr, whereas the opposite is observed in the recrystallized domains (see for comparison Harker diagrams, Fig. 3).

Furthermore, both the dehydration path of the water-rich domains and their oxygen isotope ratios point to high temperature, with temperatures between 600°C and at least 800°C in equilibrium with the mantle or the lower crust. Moreover, these fluids are not exclusively hydrous but also contain significant amounts of CO_2, which does not enter the feldspar structure, but is incorporated into carbonates, precipitating along all visible paths of fluid–feldspar interaction. The carbon of these carbonates retained a mantle isotopic signature. Finally, the fluids also contain substantial amount of halides, whose presence is in turn observed along fluid migration paths within cracks in apatite and in some apatite domains affected by interaction with those fluids.

Fluids have preferentially affected the marginal parts of the batholith (samples BH75, BH76A-B, PNS, BH80C-D, BH100F), relative to the central part (96, 171), indicating an external source. Fertile H_2O–CO_2 fluids can have either a mantle or a lower crustal origin (Hansen *et al.*, 1984; Stähle *et al.*, 1987; Wyllie & Ryabchikov, 2000; Martin & De Vito, 2005; Martin, 2006; Hansen & Harlov, 2007, 2009), both sharing several similarities. They are halogen-rich (Zaccarini *et al.*, 2004; Hansen & Harlov, 2007, 2009; Klein-BenDavid *et al.*, 2007; Frezzotti *et al.*, 2010) and thus capable of transferring several element species (Aranovich & Newton, 1996, 1997; Newton & Manning, 2008), including LILE, LREE and Pb. However, their CO_2 and H_2O activities may differ. Mantle-derived fluids can be carbonic or aqueous (Izraeli *et al.*, 2001; Perchuk *et al.*, 2002; Klein-BenDavid *et al.*, 2004, 2007; Safonov *et al.*, 2007; Santosh & Omori, 2008*a*, 2008*b*; Santosh *et al.*, 2009; Sarangi *et al.*, 2009; Tomlinson *et al.*, 2009), whereas Archaean lower crustal fluids are considered to be mainly carbonic (Hoefs & Touret, 1975; Condie *et al.*, 1982; Janardhan *et al.*, 1982; Friend, 1983, 1984, 1985; Hansen *et al.*, 1984, 1995; Stähle *et al.*, 1987; Hansen & Harlov, 2007, 2009).

In the Closepet pluton, isotopic data militate in favour of a prominent mantle component in the fluids. These could possibly have been extracted from melts derived from hydrous and carbonated mantle sources evolving towards an immiscibility gap and separating an aqueous fraction (Perchuk *et al.*, 2002; Klein-BenDavid *et al.*, 2004, 2007; Safonov *et al.*, 2007).It seems that after complete magma crystallization, the Closepet batholith still exhibited open-system behaviour, at least for fluid percolation. The conduit that favoured and controlled magma ascent and emplacement may have remained active after granite crystallization. The granite was emplaced in a major shear zone that separates two terranes (Moyen *et al.*, 2003). Generally such shear zones are supposed to be rooted deep in the mantle (Pili *et al.*, 1997*a*, 1997*b*). The mantle is frequently uplifted beneath the shear zone and hot fluids accompany and precede the mantle upwelling (Martin & Piwinskii, 1972; Woolley, 1987; Bonatti, 1990; Wyllie & Ryabchikov, 2000; Martin & De Vito, 2005; Martin, 2006). An input from crust-related fluids, however, cannot be precluded. Assuming that the two types of fluid used the same migration path, we suggest that they remained separate and probably did not significantly mix. The data collected on recrystallized feldspar domains argue for a prominent role played by a mantle fluid.

ACKNOWLEDGEMENTS

We are grateful for discussions of our work with many researchers who provided stimulating advice; we thank: R. Macdonald for redirecting our ideas from magma differentiation towards fluid interaction; J. Touret for his guidance on the Closepet thin sections, allowing us to

recognize melt inclusions in igneous feldspar domains; R. Martin for discussion of the composition of mantle-derived fluids; T. Kawamoto and K. Makino for discussion on the method used. We appreciate thoughtful and constructive reviews by J. Touret, B. Yardley and an anonymous reviewer. R. Macdonald is gratefully acknowledged for peer review and both English style and grammar correction; M. Wilson for efficient editorial handling and very helpful comments.

FUNDING

The work has been done within the framework of IGCP-SIDA 599 and has been funded by IGSci PASci 'Hybrid' and IGSci PASci-CNRS-UMR 6524-LMV project: 'Equilibration and re-equilibration processes in Archaean granites'.

SUPPLEMENTARY DATA

Supplementary data for this paper are available at *Journal of Petrology* online.

REFERENCES

Aranovich, L. Y. & Newton, R. C. (1996). H_2O activity in concentrated NaCl solutions at high pressures and temperatures measured by the brucite–periclase equilibrium. *Contributions to Mineralogy and Petrology* **125**, 200–212.

Aranovich, L. Y. & Newton, R. C. (1997). H_2O activity in concentrated KCl solutions at high pressures and temperatures measured by the brucite–periclase equilibrium. *Contributions to Mineralogy and Petrology* **127**, 261–271.

Banerjee, S., Gregory, R. T., Richards, I. & Ferguson, K. (2007). Oxygen isotope data from hydrothermally altered Archaean plutons: constraints on the isotopic evolution of the hydrosphere. *Geological Society of America, Abstracts with Programs* **39**, 14.

Blancher, S. (2004). La source des granites tardi-Archéens: manteau enrichi ou contamination crustale? Approche à l'aide des isotopes de l'oxygène. Masters Thesis, Université Blaise Pascal, Clermont-Ferrand, 50 p.

Bonatti, E. (1990). Not so hot 'hot spots' in the oceanic mantle. *Science* **250**, 107–111.

Brady, J. B. & Yund, R. A. (1983). Interdiffusion of K and Na in alkali feldspar: homogenization experiments. *American Mineralogist* **68**, 106–111.

Buhl, D. (1987). U-Pb und Rb-Sr Altersbestimmungen und Untersuchugen zum Strontiumisotopenaustausch an Granuliten Südindiens. Unpublished PhD Thesis, Universität Münster.

Chadwick, B., Vasudev, V. N. & Hegde, G. V. (2000). The Dharwar Craton, southern India, interpreted as the result of late Archaean oblique convergence. *Precambrian Research* **99**, 91–111.

Chappell, B. W. & White, A. J. R. (1974). Two contrasting granite types. *Pacific Geology* **8**, 173–184.

Cherniak, D. J. (2002). Ba diffusion in feldspar. *Geochimica et Cosmochimica Acta* **66**, 1641–1650.

Christoffersen, R., Yund, R. A. & Tullis, J. (1983). Inter-diffusion of K and Na in alkali feldspars: diffusion couple experiments. *American Mineralogist* **68**, 1126–1133.

Cole, D. R. & Chakraborty, S. (2001). Rates and mechanisms of isotopic exchange. In: Valley, J. W. & Cole, D. R. (eds) *Stable Isotope Geochemistry. Mineralogical Society of America, Reviews in Mineralogy* **43**, 82–223.

Cole, D. R., Larson, B., Riciputi, L. R. & Mora, C. I. (2004). Oxygen isotope zoning profiles in hydrothermally altered feldspars: Estimating the duration of water–rock interaction. *Geology* **32**, 29–32.

Condie, K. C., Allen, P. & Narayana, B. L. (1982). Geochemistry of the Archaean low- to high-grade transition zone, Southern India. *Contributions to Mineralogy and Petrology* **81**, 157–167.

Cressie, N. A. C. (1990). The origins of Kriging. *Mathematical Geology* **22**, 239–252.

Deines, P. (1989). Stable isotope variations in carbonatites. In: Bell, K. (ed.) *Carbonatites: Genesis and Evolution*. London: Unwin Hyman, pp. 301–359.

Divakara Rao, V., Aswathanarayana, V. U. & Quereshy, M. N. (1972). Trace element geochemistry of the Closepet granite, Mysore State, India. *Mineralogical Magazine* **38**, 678–686.

Domonik, A., Słaby, E. & Śmigielski, M. (2010). The Hurst exponent as a tool for the description of magma field heterogeneity reflected in the geochemistry of growing crystals. *Acta Geologica Polonica* **60**, 437–443.

Farver, J. H. & Yund, R. A. (1990). The effect of hydrogen, oxygen, and water fugacity on oxygen diffusion in alkali feldspar. *Geochimica et Cosmochimica Acta* **54**, 2953–2964.

Feder, J. (1991). Fractal time series and fractional Brownian motion. In: Riste, T. & Sherrington, D. (eds) *Spontaneous Formation of Space–Time Structures and Criticality*. Dordrecht: Kluwer, pp. 113–135.

Fiebig, J. & Hoefs, J. (2002). Hydrothermal alteration of biotite and plagioclase as inferred from intragranular oxygen isotope- and cation-distribution patterns. *European Journal of Mineralogy* **14**, 49–60.

Finch, A. A. & Klein, J. (1999). The causes and petrological significance of cathodoluminescence emissions from alkali feldspar. *Contributions to Mineralogy and Petrology* **135**, 234–243.

Fleming, M. D. & Hoffer, R. M. (1979). *Machine processing of Landsat MSS data and LARS Technical Report 062879*. West Lafayette, IN: Laboratory for Applications of Remote Sensing, Purdue University.

Frezzotti, M. L., Simona Ferrando, S., Peccerillo, A., Petrelli, M, Tecce, F. & Perucchi, A. (2010). Chlorine-rich metasomatic H_2O–CO_2 fluids in amphibole-bearing peridotites from Injibara (Lake Tana region, Ethiopian plateau): Nature and evolution of volatiles in the mantle of a region of continental flood basalts. *Geochimica et Cosmochimica Acta* **74**, 3023–3039.

Friend, C. R. L. (1983). The link between charnockite formation and granite production: evidence from Kabbaldurga, Karnataka, South India. In: Atherton, M. P. & Gribble, C. D. (eds) *Migmatite, Melting and Metamorphism*. Nantwich: Shiva, pp. 264–76.

Friend, C. R. L. (1984). The origins of the Closepet granites and implications of crustal evolution in southern Karnataka. *Journal of the Geological Society of India* **25**, 73–84.

Friend, C. R. L. (1985). Evidence for fluid pathways through Archaean crust and the generation of the Closepet granite, Karnataka, South India. *Precambrian Research* **27**, 239–250.

Friend, C. R. L. & Nutman, A. P. (1991). SHRIMP U–Pb geochronology of the Closepet granite and Peninsular gneisses, Karnataka, South India. *Journal of the Geological Society of India* **38**, 357–368.

Gagnevin, D., Daly, J. S., Poli, G. & Morgan, D. (2005*a*). Microchemical and Sr isotopic investigation of zoned K-feldspar megacrysts: insights into the petrogenesis of a granitic system and disequilibrium crystal growth. *Journal of Petrology* **46**, 1689–1724.

Gagnevin, D., Daly, J. S., Waight, T., Morgan, D. & Poli, G. (2005*b*). Pb isotopic zoning of K-feldspar megacrysts determined by laser

ablation multiple-collector ICP-MS: insights into granite petrogenesis. *Geochimica and Cosmochimica Acta* **69**, 1899–1915.

Gao, Y., Hoefs, J., Przybilla, R. & Snow, J. E. (2006). A complete oxygen isotope profile through the lower oceanic crust, ODP Hole 735B. *Chemical Geology* **233**, 217–234.

Götze, J., Krbetschek, M. R., Habermann, D. & Wolf, D. (2000). High-resolution cathodoluminescence of feldspar minerals. In: Pagel, M., Barbin, V., Blanc, P. & Ohnenstetter, D. (eds) *Cathodoluminescence in Geosciences*. Berlin: Springer, pp. 245–270.

Graham, C. M. & Elphick, S. C. (1990). A re-examination of the role of hydrogen in Al–Si interdiffusion in feldspars. *Contributions to Mineralogy and Petrology* **104**, 481–491.

Grew, E. S. & Manton, W. I. (1984). Age of allanite from Kabbaldurga quarry, Karnataka. *Journal of the Geological Society of India* **25**, 193–195.

Hansen, E. C. & Harlov, D. E. (2007). Phosphate, silicate and fluid composition across an amphibolite- to granulite-facies transition, Tamil Nadu, India. *Journal of Petrology* **48**, 1641–1680.

Hansen, E. C. & Harlov, D. E. (2009). Orthophosphate and biotite chemistry from orthopyroxene-bearing migmatites from California and South India: The role of a fluid-phase in the evolution of granulite-facies migmatites. *Mineralogy and Petrology* **95**, 201–217.

Hansen, E. C., Newton, R. C. & Janardhan, A. S. (1984). Fluid inclusions in rocks from the amphibolite-facies gneiss to charnockite progression in southern Karnataka, India: Direct evidence concerning the fluids of granulite metamorphism. *Journal of Metamorphic Geology* **2**, 249–264.

Hansen, E. C., Newton, R. C., Janardhar, A. S. & Lindenberg, S. (1995). Differentiation of Late Archean crust in the Eastern Dharwar craton, Krishnagiri–Salem area, south India. *Journal of Geology* **103**, 629–651.

Hoefs, J. & Touret, J. (1975). Fluid inclusion and carbon isotope study from Bamble granulites (S Norway). *Contributions to Mineralogy and Petrology* **52**, 165–174.

Holten, T., Jamtveit, B., Meakin, P., Cortini, M., Blundy, J. & Austrheim, H. (1997). Statistical characteristics and origin of oscillatory zoning in crystals. *American Mineralogist* **82**, 596–606.

Hoskin, P. W. O. (2000). Patterns of chaos: Fractal statistics and the oscillatory chemistry of zircon. *Geochimica et Cosmochimica Acta* **64**, 1905–1923.

Iiyama, J. T. (1965). Influence des anions sur les équilibres d'échange d'ions Na–K dans les feldspaths alkalines à 600°C sous une pression de 1000 bars. *Bulletin de la Société Française de Minéralogie et de Cristallographie* **87**, 618–622.

Iiyama, J. T. (1968). Etude expérimentale de la distribution d'éléments en traces entre deux feldspaths. Feldspath potassique et plagioclase coexistants. I. Distribution de Rb, Cs, Sr et Ba à 600°C. *Bulletin de la Société Française de Minéralogie et de Cristallographie* **91**, 130–140.

Izraeli, E. S., Harris, J. W. & Navon, O. (2001). Brine inclusions in diamonds: a new upper mantle fluid. *Earth and Planetary Science Letters* **187**, 323–332.

Janardhan, A. S., Newton, R. C. & Hansen, E. C. (1982). The transformation of amphibolite facies gneiss to charnockite in Southern Karnataka and Northern Tamil Nadu, India. *Contributions to Mineralogy and Petrology* **79**, 130–149.

Jayananda, M. (1988). The geology and petrogenesis of the southern Closepet granite. Karnakata, South India: PhD thesis, University of Bangalore.

Jayananda, M., Martin, H. & Mahabaleswar, B. (1992). The mechanism of recycling of the Archaean continental crust: Example of the Closepet granite, Southern India. In: Radhakrishna, B. P. (ed.) *Continental Crust of South India*. Bangalore: Geological Society of India, pp. 213–223.

Jayananda, M., Martin, H., Peucat, J.-J. & Mahabaleswar, B. (1995). Late Archaean crust–mantle interactions in the Closepet granite, Southern India: evidence from Sr–Nd isotopes, major and trace element geochemistry. *Contributions to Mineralogy and Petrology* **119**, 314–329.

Jayananda, M., Miyazaki, T., Gireesh, R. V., Mahesha, N. & Kano, T. (2009). Synplutonic mafic dykes from Late Archaean granitoids in the Eastern Dharwar craton, Southern India. *Journal of the Geological Society of India* **73**, 117–130.

Jayananda, M., Moyen, J.-F., Martin, H., Peucat, J.-J., Auvray, B. & Mahabaleswar, B. (2000). Late Archaean (2550–2520 Ma) juvenile magmatism in the Eastern Dharwar craton, southern India: constraints from geochronology, Nd–Sr isotopes and whole rock geochemistry. *Precambrian Research* **99**, 225–254.

Johnson, E. A. & Rossman, G. R. (2003). The concentration and speciation of hydrogen in feldspars using FTIR and ^{1}H MAS NMR spectroscopy. *American Mineralogist* **88**, 901–911.

Johnson, E. A. & Rossman, G. R. (2004). A survey of hydrous species and concentrations in igneous feldspars. *American Mineralogist* **89**, 586–600.

Klein-BenDavid, O., Izraeli, E. S., Hauri, E. & Navon, O. (2004). Mantle fluid evolution—a tale of one diamond. *Lithos* **77(1–4)**, 243–253.

Klein-BenDavid, O., Izraeli, E. S., Hauri, E. & Navon, O. (2007). Fluid inclusions in diamonds from the Diavik mine, Canada and the evolution of diamond-forming fluids. *Geochimica et Cosmochimica Acta* **71**, 723–744.

Kronenberg, A. K., Yund, R. A. & Rossman, G. R. (1996). Stationary and mobile hydrogen defects in potassium feldspar. *Geochimica et Cosmochimica Acta* **60**, 4075–4094.

Labotka, T. C., Cole, D. R., Fayek, M., Riciputi, L. R. & Stadermann, F. J. (2004). Coupled cation and oxygen-isotope exchange between alkali feldspar and aqueous chloride solution. *American Mineralogist* **89**, 1822–1825.

Lagache, M. & Weisbrod, A. (1977). The system two alkali feldspars–KCl–NaCl–H_2O at moderate to high temperatures and low pressures. *Contributions to Mineralogy and Petrology* **62**, 77–101.

Mandelbrot, B. B. & Van Ness, J. W. (1968). Fractional Brownian motions, fractional noises and applications. *SIAM Review* **10**, 422–437.

Marfunin, A. S. & Bershov, L. V. (1970). Electron-hole centers in feldspars and their possible crystal chemical and petrological significance. *Doklady Akademii Nauk SSSR* **193**, 412–414 (in Russian).

Martin, H., Moyen, J.-F. & Rapp, R. (2010). The sanukitoid series: magmatism at the Archaean–Proterozoic transition. *Transactions of the Royal Society of Edinburgh, Earth Sciences* **100**, 15–33.

Martin, R. F. (2006). A-type granites of crustal origin ultimately result from open-system fenitization-type reactions in an extensional environment. *Lithos* **91**, 125–136.

Martin, R. F. & De Vito, C. (2005). The patterns of enrichment in felsic pegmatites ultimately depend on tectonic setting. *Canadian Mineralogist* **43**, 2027–2048.

Martin, R. F. & Piwinskii, A. J. (1972). Magmatism and tectonic settings. *Journal of Gephysical Research* **77**, 4966–4975.

Meen, J. K., Rogers, J. J. W. & Fullagar, P. D. (1992). Lead isotopic compositions in the western Dharwar craton, southern India: evidence for distinct middle Archaean terrains in a late Archaean craton. *Geochimica et Cosmochimica Acta* **56**, 2455–2470.

Moyen, J.-F. (2000). Le magmatisme granitique à la transition Archéen–Protérozoïque: Exemple du craton de Dharwar, Inde du

Sud (Massif de Closepet et intrusions associées). Université PhD thesis, Université Blaise Pascal, Clermont-Ferrand, 503 p.

Moyen, J.-F. (2009). High Sr/Y and La/Yb ratios: the meaning of the 'adakitic signature'. *Lithos* **112**, 556–574.

Moyen, J.-F., Martin, H. & Jayananda, M. (1997). Origine du granite fini-Archéen de Closepet (Inde du Sud): apports de la modélisation géochimique du comportement des éléments en traces. *Comptes Rendus de l'Académie des Sciences* **325**, 659–664.

Moyen, J.-F., Martin, H. & Jayananda, M. (2001*a*). Multi-element geochemical modelling of crust–mantle interactions during late-Archaean crustal growth: the Closepet granite (South India). *Precambrian Research* **112**, 87–105.

Moyen, J.-F., Martin, H., Jayananda, M. & Auvray, B. (2003). Late Archaean granites: a typology based on the Dharwar Craton (India). *Precambrian Research* **127**, 103–123.

Moyen, J.-F., Nédélec, A., Martin, H. & Jayananda, M. (2001*b*). Contrasted granite emplacement modes within an oblique crustal section: the Closepet Granite, South India. *Physics and Chemistry of the Earth (A)* **26**, 295–301.

Nakamura, E. & Kushiro, I. (1998). Trace element diffusion in jadeite and diopside melts at high pressures and its geochemical implication. *Geochimica et Cosmochimica Acta* **62**, 3151–3160.

Nakano, S., Makino, K. & Eriguchi, T. (2001). Microtexture and water content of alkali feldspar by Fourier-transform infrared microspectroscopy. *Mineralogical Magazine* **65**, 675–683.

Nash, W. P. & Crecraft, H. R. (1985). Partition coefficients for trace elements in silicic magmas. *Geochimica and Cosmochimica Acta* **49**, 2309–2322.

Neuser, R. D., Bruhn, F., Götze, J., Habermann, D. & Richter, D. K. (1995). Kathodolumineszenz: Methodik und Anwendung. *Zentralblatt für Geologie und Paläontologie, Teil* **I(1/2)**, 287–306.

Newton, R. C. (1990). The late Archaean high-grade terrain of South India and the deep structure of the Dharwar craton. In: Salisbury, M. H. & Fountain, D. M. (eds) *Exposed Cross-sections of the Continental Crust*. Dordrecht: Kluwer, pp. 305–326.

Newton, R. C. & Manning, C. E. (2008). Solubility of corundum in the system Al_2O_3–SiO_2–H_2O–NaCl at 800°C and 10 kbar. *Chemical Geology* **248**, 250–261.

Niedermeier, D. R. D., Putnis, A., Geisler, T., Golla-Schindler, U. & Putnis, C. V. (2009). The mechanism of cation and oxygen isotope exchange in alkali feldspars under hydrothermal conditions. *Contributions to Mineralogy and Petrology* **157**, 65–76.

Nutman, A. J., McGregor, V. R., Friend, C. R. L., Bennett, V. C. & Kinny, P. D. (1996). The Itsaq gneiss complex of southern Greenland; the world's most extensive record of early crustal evolution (3900–3600 Ma). *Precambrian Research* **78**, 1–39.

Parsons, I. (1978). Feldspars and fluids in cooling plutons. *Mineralogical Magazine* **42**, 1–17.

Parsons, I. & Lee, M. R. (2009). Mutual replacement reactions in alkali feldspars I: microtextures and mechanisms. *Contributions to Mineralogy and Petrology* **157**, 641–662.

Parsons, I., Magee, C. W., Allen, C. M., Shelley, J. M. G. & Lee, M. R. (2009). Mutual replacement reactions in alkali feldspars II: trace element partitioning and geothermometry. *Contributions to Mineralogy and Petrology* **157**, 663–687.

Perchuk, L. L., Safonov, O. G., Yapaskurt, V. O. & Barton, J. M. (2002). Crystal–melt equilibria involving potassium-bearing clinopyroxene as indicator of mantle-derived ultrahigh-potassic liquids: an analytical review. *Lithos* **60**, 89–111.

Perugini, D. & Poli, G. (2004). Analysis and numerical simulation of chaotic advection and chemical diffusion during magma mixing: petrological implications. *Lithos* **78**, 43–66.

Perugini, D., Poli, G. & Gatta, G. D. (2002). Analysis and simulation of magma mixing processes in 3D. *Lithos* **65**, 313– 330.

Perugini, D., Poli, G. & Mazzuoli, R. (2003). Chaotic advection, fractals and dffusion during mixing of magmas: evidence from lava flows. *Journal of Volcanology and Geothermal Research* **124**, 255–279.

Perugini, D., Poli, G. & Valentini, L. (2005). Strange attractors in plagioclase oscillatory zoning: petrological implications. *Contributions to Mineralogy and Petrology* **149**, 482–497.

Perugini, D., De Campos, C. P., Dingwell, D. B., Petrelli, M. & Poli, D. (2008). Trace element mobility during magma mixing: Preliminary experimental results. *Chemical Geology* **256**, 146–157.

Peters, E. E. (1994). *Fractal Market Analysis: Applying Chaos Theory to Investment and Economics*. New York: John Wiley.

Pili, E., Ricard, Y., Lardeaux, J.-M. & Sheppard, S. M. F. (1997*a*). Lithospheric shear zone and mantle–crust connections. *Tectonophysics* **280**, 15–29.

Pili, E., Sheppard, S. M. F., Lardeaux, J.-M., Martelat, J.-E. & Nicollet, C. (1997*b*). Fluid flow vs. scale of shear zones in the lower continental crust and the granulite paradox. *Geology* **25**, 15–18.

Plümper, O. & Putnis, A. (2009). The complex hydrothermal history of granitic rocks: Multiple feldspar replacement reactions under subsolidus conditions. *Journal of Petrology* **50**, 967–987.

Putnis, A. (2002). Mineral replacement reactions: from macroscopic observations to microscopic mechanisms. *Mineralogical Magazine* **66**, 689–708.

Putnis, A. (2009). Mineral replacement reactions. In: Oelkers, E. H. & Scott, J. (eds) *Thermodynamics and Kinetics of Water–Rock Interaction. Mineralogical Society of America and Geochemical Society, Reviews in Mineralogy and Geochemistry* **70**, 87–124.

Putnis, C. V., Tsukamoto, K. & Nishimura, Y. (2005). Direct observations of pseudomorphism: compositional and textural evolution at a fluid–solid interface. *American Mineralogist* **90**, 1909–1912.

Putnis, A., Hinrichs, R., Putnis, C. V., Golla-Schindler, U. & Collins, L. G. (2007). Hematite in porous red-clouded feldspars: Evidence of large-scale crustal fluid–rock interaction. *Lithos* **95**, 10–18.

Radhakrishna, B. P. (1958). On the nature of certain brick-red zones in Closepet granite. *Mysore Geological Department Records* **48**, 61–73.

Rapp, R. P., Laporte, D., Martin, H. & Shimizu, N. (2006). Experimental insights into slab–mantle interactions in subduction zones: Melting of adakite-metasomatized peridotite and the origin of the 'arc signature'. *Geochimica et Cosmochimica Acta* **70(18, Supplement 1)**, A517.

Safonov, O. G., Perchuk, L. L. & Litvin, Y. A. (2007). Melting relations in the chloride–carbonate–silicate systems at high-pressure and the model for formation of alkalic diamond forming liquids in the upper mantle. *Earth and Planetary Science Letters* **253**, 112–128.

Santos, R. V. & Clayton, R. N. (1995). Variations of oxygen and carbon isotopes in carbonatites: a study of Brazilian alkaline complexes. *Geochimica et Cosmochimica Acta* **59**, 1339–1352.

Santosh, M. & Omori, S. (2008*a*). CO_2 flushing: A plate tectonic perspective. *Gondwana Research* **13**, 86–102.

Santosh, M. & Omori, S. (2008*b*). CO_2 windows from mantle to atmosphere: Models on ultrahigh-temperature metamorphism and speculations on the link with melting of snowball Earth. *Gondwana Research* **14**, 82–96.

Santosh, M., Maruyama, S. & Omori, S. (2009). A fluid factory in solid Earth. *Lithosphere* **1**, 29–33.

Sarangi, S., Sarkar, A., Srinivasan, R. & Patel, S. C. (2009). Mantle origin for auriferous CO_2 rich fluids at the Archaean lode gold deposit of Ajjenahalli, Chitradurga greenstone belt, southern India. *Geochimica et Cosmochimica Acta, Goldschmidt Conference Abstracts* A1158.

Shimizu, K., Komiya, T., Hirose, K., Shimizu, N. & Maruyama, S. (2001). Cr-spinel, an excellent micro-container for retaining primitive melts—implications for a hydrous plume origin for komatiites. *Earth and Planetary Science Letters* **189**, 177–188.

Shirey, S. B. & Hanson, G. N. (1984). Mantle derived Archaean monzodiorites and trachyandesites. *Nature* **310**, 222–224.

Słaby, E. (1992). Changes in the structural state of secondary albites during progressive alteration. *Neues Jahburch für Mineralogie, Monathefte* **H7**, 321–335.

Słaby, E. (1994). TAS classification—how to overcome problems with post-magmatic feldspar formation in Permian volcanic rocks. *Zentralblatt für Geologie und Paläontologie* **I(5–6)**, 541–552.

Słaby, E., Lensch, G. & Mihm, A. (1988). Alkali metasomatism of 'plagiaplites' from Tholey (Saarland, W. Germany); Part 1, Feldspars. *Neues Jahrbuch für Mineralogie, Abhandlungen* **159(3)**, 237–247.

Słaby, E., Galbarczyk-Gąsiorowska, L., Seltmann, R. & Müller, A. (2007). Alkali feldspar megacryst growth: geochemical modelling. *Mineralogy and Petrology* **68**, 1–29.

Słaby, E., Śmigielski, M., Domonik, A., Simon, K. & Kronz, A. (2011). Chaotic three-dimensional distribution of Ba, Rb and Sr in feldspar megacrysts grown in an open magmatic system. *Contributions to Mineralogy and Petrology* **162**, 909–927.

Słaby, E., Götze, J., Wörner, G., Simon, K., Wrzalik, R. & Śmigielski, M. (2008). K-feldspar phenocrysts in microgranular magmatic enclaves: A cathodoluminescence and geochemical study of crystal growth as a marker of magma mingling dynamics. *Lithos* **105**, 85–97.

Śmigielski, M., Słaby, E. & Domonik, A. (2011). Digital Concentration-Distribution Models - tools for a describing heterogeneity of the hybridized magmatic mass as reflected in elemental concentration of growing crystal. *Acta Geologica Polonica* (accepted).

Srikantappa, C., Raith, M. & Touret, J.L.R. (1992). Synmetamorphic high-density carbonic fluids in the lower crust: Evidence from Nilgiri granulites, Southers India. *Journal of Petrology* **33**, 733–760.

Stähle, H. J., Raith, M., Hoernes, S. & Delfs, A. (1987). Element mobility during incipient granulite formation at Kabbaldurga, Southern India. *Journal of Petrology* **28**, 803–834.

Stern, R. A., Nesbitt, R. W. & McCulloch, M. T. (1989). Geochemistry and petrogenesis of siliceous high magnesian basalts of the Archaean and early Proterozoic. In: Crawford, A. R. (ed.) *Boninites and Related Rocks*. London: Unwin Hyman, pp. 148–173.

Subba Rao, M. V., Divakara Rao, V., Govil, P. K., Balaram, V. & Pantulu, G. V. C. (1992). Geochemical and Sr isotopic signatures in the 2·6 By Lepakshi granite, Anantapur district, Andhra Pradesh: implications for its origin and evolution. *Indian Minerals* **46**, 289–302.

Taylor, H. P. (1978). Oxygen and hydrogen isotope studies of plutonic granitic rocks. *Earth and Planetary Science Letters* **38**, 177–210.

Taylor, H. P., Frechen, J. & Degens, E. T. (1967). Oxygen and carbon isotope studies of carbonatites from the Laacher See District, West Germany and the Alno District, Sweden. *Geochimica et Cosmochimica Acta* **31**, 407–430.

Taylor, P. N., Chadwick, B., Moorbath, S., Ramakrishanan, M. & Viswanatha, M. N. (1984). Petrography, chemistry and isotopic ages of Peninsular gneisses, Dharwar acid volcanics and Chitradurga granites with special reference to Archaean evolution of Karnataka craton, southern India. *Precambrian Research* **3**, 349–375.

Tichomirowa, M., Grosche, G., Götze, J., Belyatsky, B. V., Savva, E. V., Keller, J. & Todt, W. (2006). The mineral isotope composition of two Precambrian carbonatite complexes from the Kola Alkaline Province—Alteration versus primary magmatic signatures. *Lithos* **91**, 229–249.

Tomlinson, E. L., Müller, W. & Edinburgh Ion Microprobe Facility (EIMF) (2009). A snapshot of mantle metasomatism: Trace element analysis of coexisting fluid (LA-ICP-MS) and silicate (SIMS) inclusions in fibrous diamonds. *Earth and Planetary Science Letters* **279**, 362–372.

Touret, J. L. R. (2005). Ultrahigh-temperature granitoids in southern India: Fuelling the fluid debate about the lower continental crust. *Comptes Rendus Géoscience* **337**, 1303–1304.

Turcotte, D. L. (1997). *Fractals and Chaos in Geology and Geophysics*. Cambridge: Cambridge University Press.

Van den Kerkhof, A. M. & Hein, U. F. (2001). Fluid inclusion petrography. *Lithos* **55**, 27–47.

Van den Kerkhof, A. M., Kronz, A., Simon, K. & Scherer, T. (2004). Fluid-controlled quartz recovery in granulite as revealed by cathodoluminescnec and trace element analysis (Bamble sector, Norway). *Contributions to Mineralogy and Petrology* **146**, 637–652.

Vernon, R. H. (1986). K-feldspar megacrysts in granites—phenocrysts, not porphyroblasts. *Earth-Science Reviews* **23**, 1–63.

Vernon, R. H. & Paterson, S. R. (2008). How late are K-feldspar megacrysts in granites? *Lithos* **104**, 327–336.

Wiechert, U. & Hoefs, J. (1995). An excimer laser-based micro-analytical preparation technique for *in situ* oxygen isotope analysis of silicate and oxide minerals. *Geochimica et Cosmochimica Acta* **59**, 4093–4101.

Wiechert, U., Fiebig, J., Przybilla, R., Xiao, Y. & Hoefs, J. (2002). Excimer laser isotope-ratio-monitoring mass spectrometry for *in situ* oxygen isotope analysis. *Chemical Geology* **182**, 179–194.

Woolley, A. R. (1987). Lithosphere metasomatism and the petrogenesis of the Chilwa Province of alkaline igneous rocks and carbonatites, Malawi. *Journal of African Earth Sciences* **6**, 891–898.

Wyllie, P. J. & Ryabchikov, I. D. (2000). Volatile components, magmas, and critical fluids in upwelling mantle. *Journal of Petrology* **41**, 1195–1206.

Yund, R. A. & Anderson, T. F. (1978). Oxygen isotope exchange between feldspar and fluid as a function of fluid pressure. *Geochimica et Cosmochimica Acta* **42**, 235–239.

Zaccarini, F., Stumpfl, E. F. & Garuti, G. (2004). Zirconolite and Zr–Th–U minerals in chromitites of the Finero complex, Western Alps, Italy: evidence for carbonatite-type metasomatism in a subcontinental mantle plume. *Canadian Mineralogist* **42**, 1825–1845.